Quantifying Segregation Efficiency in the Active Layer Using an Idealized Lens-Resolving Numerical Model

by

Azadeh Dadfarin

A thesis accepted and approved in partial fulfillment of the

requirements for the degree of

Master of Science

in Earth Sciences

Thesis Committee:

Joshua Roering, Chairperson

Leif Karlstrom, Member

Susheel Adusumilli, Member

University of Oregon

Winter 2026

THESIS ABSTRACT

Azadeh Dadfarin

Master of Science in Earth Science

Title: Quantifying Segregation Efficiency in the Active Layer Using an Idealized Lens-Resolving Numerical Model

The active layer, the seasonally thawed soil overlying permafrost, is a Key uppermost ground layer, controlling landscape stability, hydrological cycles, and the thermal regime of underlying permafrost. These active-layer dynamics have direct implications for the durability of infrastructure in permafrost regions. A key process governing active layer dynamics is frost heave, the vertical displacement of sediment caused by the formation of ice lenses during freezing. Ice lenses form within the frozen fringe, a zone of partial ice saturation where water migrates toward a freezing front. This migration results in gradually building up layers of segregated ice, a process influenced by temperature gradients, soil properties, and overburden pressure. However, predicting ice lens distributions is computationally intensive due to the complex interactions of thermal, hydraulic, and mechanical factors that vary across large spatial scales. To bridge this scale gap, we develop a physically based parameterization for segregation efficiency (E). This metric quantifies the proportion of the total heat flux across a freezing front that is converted into latent heat for ice lens growth, offering a measure of the thermodynamic efficiency of segregation. This parameter provides a potential bridge between microscale energy partitioning and macroscale frost-heave dynamics. We use a lens-resolving frost heave model that constrains segregation efficiency by analyzing its dependence on ice saturation, permeability, soil freezing characteristics, and heat flux. The model incorporates key thermal boundary conditions, including geothermal heat flux and surface heat flux, which are critical for simulating permafrost behavior.

It also accounts for mechanical loading through an effective-stress (contact-stress) framework, enabling physically constrained parameterizations of E. Our results demonstrate that for $Q_s > Q_g$, segregation efficiency decreases nonlinearly with increasing surface heat flux, with a steep decline at low Q_s and an asymptotic approach at Q_s. Increasing ice saturation rapidly reduces permeability under the prescribed power-law relations, limiting water supply and suppressing E. These findings are directly relevant for improving the accuracy of large-scale permafrost modeling and understanding climate feedback loops.

ACKNOWLEDGMENTS

I would like to express my sincere gratitude to Professor Josh Roaring for his guidance, support, and assistance in preparing this manuscript. I am also grateful to my committee members, Dr. Leif Karlstrom and Dr. Susheel Adusumilli, for their time, insight, and constructive comments, which greatly strengthened this work. I would also like to express my sincere appreciation to Professor Paul Wallace, Dr. Thomas Giachetti, Professor Samantha Hopkins, Professor Josef Dufek, and Professor Matthew Polizzotto for their exceptional support and understanding during a particularly challenging period of my graduate studies. Their thoughtfulness, patience, and willingness to offer guidance and encouragement, especially during the process of changing advisors and managing academic responsibilities, were invaluable and helped me navigate these challenges and continue my research. I also thank Mrs. Marla Trox, Graduate Program Coordinator, for her invaluable assistance and support throughout my graduate studies.

Last but not least, I am deeply grateful to my husband, Max, for his constant encouragement, patience, and unwavering support throughout this journey. I also thank my family for their continued support and belief in me.

DEDICATION

This work is dedicated to the thousands of Iranian people whose lives were taken in the pursuit of freedom, dignity, and justice.

Their lives and deaths form part of a history that calls for moral responsibility, human solidarity, and the greater awareness that shapes collective understanding and reality.

Table of Contents

Chapter **Page**

List of Figures

Figure **Page**

List of Tables

Table **Page**

I. INTRODUCTION AND BACKGROUND

Permafrost, the ground that remains frozen for at least two consecutive years, is a critical component of cold-region landscapes, governing their stability and function. When permafrost begins to thaw, particularly in ice-rich soils, it can lead to ground subsidence and slope instability, alter drainage patterns, damage infrastructure, and release significant amounts of stored carbon as CO_2 and CH_4, generating an amplifying climate feedback loop that accelerates global warming (Schuur et al., 2015). Recent assessments suggest that approximately 44% of the heat absorbed by Arctic permafrost is consumed as latent heat for ground ice melt, acting as a major yet vulnerable heat sink within the global climate system (Nitzbon et al., 2023). Consequently, this underscores the necessity of quantifying the drivers and impacts of ground ice melt, particularly in ice-rich regions where significant thaw triggers accelerated carbon feedback loops (Turetsky et al., 2020). This vulnerability is heightened because permafrost underlies vast regions of the Northern Hemisphere (Figure 1), and observations indicate widespread permafrost warming across these regions, with particularly large warming rates in the Arctic, increasing the likelihood of thaw.

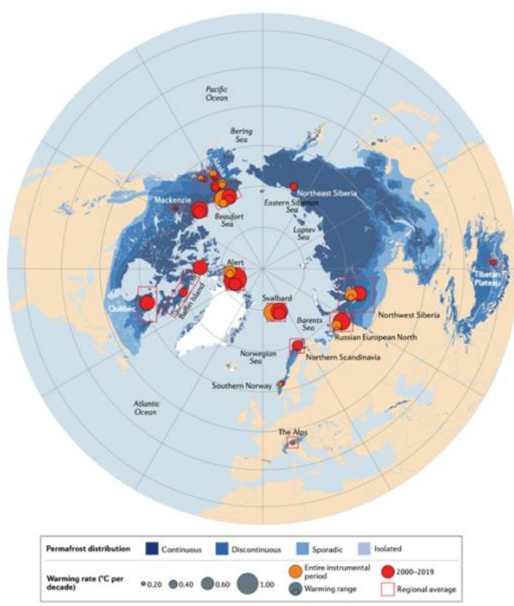

Figure 1. Northern Hemisphere Permafrost Distribution and Temperature Trends.
Northern Hemisphere permafrost zones (shaded) and permafrost temperature trend magnitudes from monitoring sites (symbol size), shown for the full instrumental period and 2000–2019 (reproduced from Smith et al., 2022).

Overlying permafrost is the active layer, the seasonally thawed zone that mediates exchanges of energy, water, and carbon between the atmosphere and permafrost. Variations in its thickness influence landscape stability, hydrological processes, carbon cycling, and infrastructure resilience in permafrost regions (Smith et al., 2022). These dynamics present major geotechnical challenges for transportation infrastructure; in ice-rich permafrost embankments, thaw settlement and associated uneven deformation are a major cause of damage (Yang et al., 2021). As an example, using 38 years of daily streamflow observations from the Kuparuk River on Alaska's North Slope, Cooper et al. (2023) infer ongoing active-layer thickening at the basin scale, with estimated increases of ~0.29 ± 0.31 cm yr^{-1} over 1990–2020 and ~0.53 ± 0.37 cm yr^{-1} over 2002–2020, indicating a larger active layer thickening rate in the more recent period. In addition, they note that as the active layer deepens with permafrost thaw, it can store more water and sustain greater subsurface flow and baseflow during dry periods, linking thaw-driven thickening to measurable hydrologic change. Such climate-driven thaw of near-surface permafrost threatens cold-region infrastructure, with mid-century (2041–2060) projections suggesting significant loss of structural bearing capacity due to the degradation of ice-rich near-surface soils (Hjort et al., 2018).

A key process influencing active layer and permafrost stability is frost heave, which occurs when water in porous soils freezes and forms ice lenses that segregate from the soil matrix, causing upward displacement of the ground surface (Taber, 1930). Figure 2A-B provides a conceptual illustration of frost heave in permafrost regions, highlighting how ice lens formation within the active layer and near the permafrost table produces wintertime heave and (with thaw) leads to surface deformation through repeated freeze–thaw cycles. A process-resolving example of the resulting freeze–thaw surface-displacement signal, including a lensing versus suppressed-lensing control, is shown in Appendix A (Fig. 24).

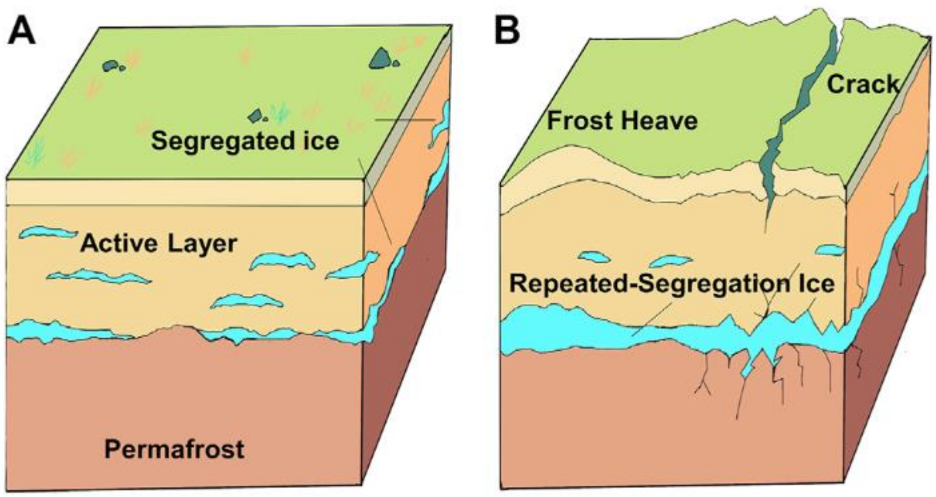

Figure 2. Frost Heave and Segregated Ice Formation.
Conceptual schematic of frost heave processes and segregated ice formation in permafrost terrain. ***(A)*** *Segregated ice initially forms within the active layer during seasonal freezing, with ice lenses preserved near the permafrost table following freeze–thaw cycles.* ***(B)*** *Under sustained cooling, repeated ice segregation leads to ice-lens thickening, surface uplift (frost heave), and the development of frost cracks. The schematic illustrates the vertical coupling between the active layer and underlying permafrost that controls frost-heave-driven deformation (Reproduced from Fu et al., 2022.)*

Frost heave is not merely a consequence of in situ pore-water freezing; rather, it is fundamentally an open-system process that often involves the migration of unfrozen water toward freezing fronts, where it freezes to form discrete ice lenses (Taber, 1930). This open-system nature is underscored by field observations where surface elevation changes deviate from predictions based on a simple, conduction-only Stefan-type freezing/thaw-front estimate (Kurylyk & Hayashi, 2016), and are instead modulated by hydrological inputs, indicating significant mass redistribution (Gruber, 2020). Migration of unfrozen water toward freezing fronts and lens formation is driven by the balance between latent heat released during freezing and conductive heat flow that drives the thermal gradient. The latent heat required for phase change during freezing or thawing far exceeds the sensible heat required to change soil temperature, making ice content a dominant control on freezing rates and active layer thickness (Clayton et al., 2021). Consequently, the amount and spatial heterogeneity of ground ice (expressed through active-layer water storage) strongly modulate seasonal heave–subsidence patterns, and multi-year deformation trends can indicate permafrost thaw that increases active-layer water storage (Chen et al., 2020b).

Specifically, to understand water migration, one must consider the pore-scale structure. Frozen soil is a three-phase system, as illustrated in Figure 3, composed of solid particles, ice, and residual liquid water, which the remaining liquid phase can persist below 0 °C and enable continued hydraulic transport (Yu et al., 2024)**.**

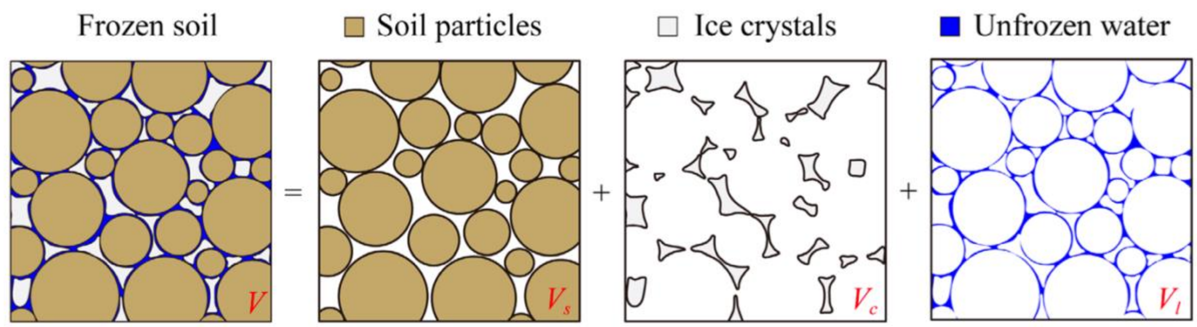

Figure 3. Frozen Soil as a Three-Phase Mixture.
Schematic illustration of frozen soil as a three-phase mixture of soil particles, ice crystals, and unfrozen water. (Reproduced from Yu et al., 2024).

Additionally, ground ice in permafrost exhibits diverse morphologies (Figure 4) depending on thermal history, sediment type, and hydrological conditions. Among these, most ground ice is in the form of thin, sub-horizontal sheets (ice lenses) (Heginbottom et al. 2012) and is most directly associated with frost heave (Taber, 1930), making it the focus of this study.

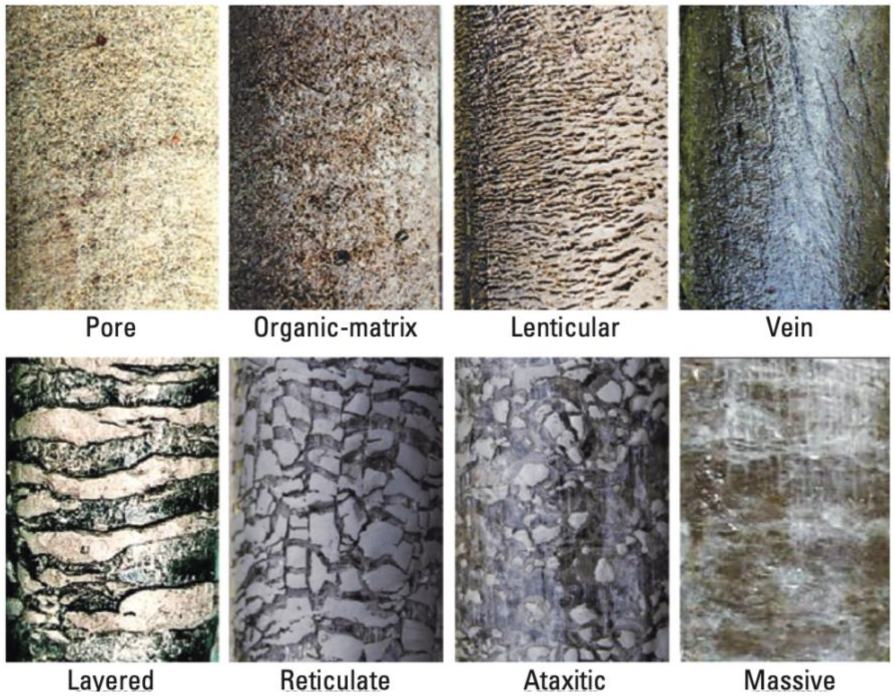

Figure 4. Segregated Ice Cryostructure Types.
Illustrations of eight types of segregated ice (cryostructures) observed in permafrost. Reproduced from Heginbottom et al. (2012), Fig. 10; image provided by M.T. Jorgenson (ABR, Inc.).

Ice lenses form within the frozen fringe, the partially frozen transition zone between unfrozen soil and fully frozen ground, where liquid water and ice coexist (Figure 5). Within this region, pores are only partially ice-filled, allowing unfrozen water to migrate in response to thermal and pressure gradients. As a result, in the frozen fringe, permeability decreases as porous ice forms, yet moisture can continue migrating under pressure gradients associated with depressed pore-water pressure; because permeability is low, moisture can accumulate and form ice lenses behind the freezing front (Fu et al., 2022).

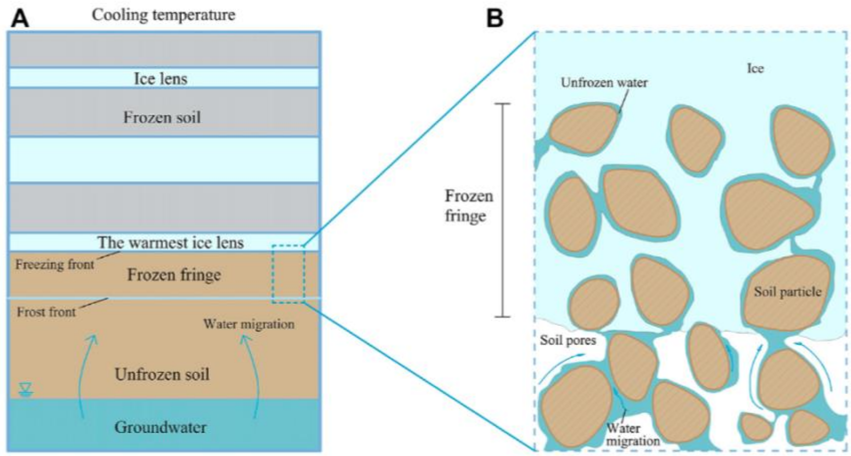

Figure 5. Frozen Fringe Structure and Water Migration.
Schematic diagram of the frozen fringe during soil freezing: (A) relative position of frozen, frozen-fringe, and unfrozen zones; (B) magnified view of the frozen-fringe zone. Reproduced from Fu et al. (2022), Fig. 4

Early experiments, such as the classic work by Taber (1930), provided clear evidence for the formation of discrete ice lenses during soil freezing and revealed the existence of a partially frozen fringe beneath actively growing lenses. In a classic step-freezing experiment, Taber (1930) demonstrated that repeated freezing leads to the development of multiple ice lenses within a soil column, separated by zones of partially frozen sediment. Figure 6 shows a photograph from this experiment. As illustrated in the accompanying modern schematic, this partially frozen fringe consists of a mixture of soil particles, ice, and unfrozen water and serves as the pathway through which water is transported toward the growing ice lens (Rempel, 2007).

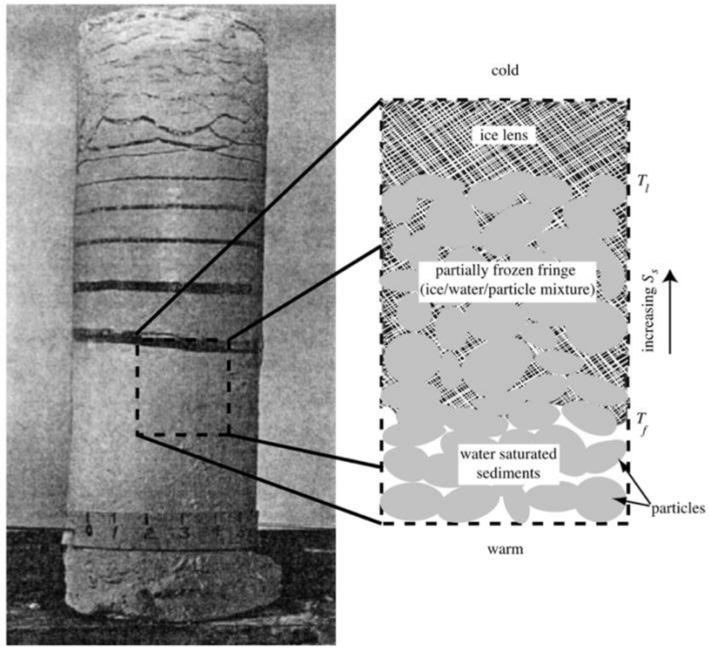

Figure 6. Ice Lens Formation in a Step-Freezing Experiment.
Formation of discrete ice lenses during a controlled step-freezing laboratory experiment. The photograph shows multiple ice lenses developing within a soil column, while the accompanying schematic highlights the partially frozen fringe that forms beneath the lowest active ice lens. This fringe consists of a mixed phase of soil particles, ice, and unfrozen water and represents the zone through which water is supplied to the growing lens. Reproduced from Taber (1930).

The existence and dynamics of this frozen fringe have been confirmed in field conditions through detailed monitoring of water content redistribution using neutron scattering, providing quantitative evidence for the suction of water from unfrozen layers and its accumulation in the partially frozen zone (Fukuda and Kinosita, 1985), and in controlled laboratory settings via X-ray radiography, which clearly images the evolving ice-lens distribution and, when combined with co-located temperature measurements, enables determination of the frozen fringe thickness and temperature range (Akagawa, 1988). Accordingly, here, cryo-suction, the movement of water toward colder regions driven by thermodynamic and hydraulic gradients, plays a central role in supplying water to growing ice lenses (Meyer et al., 2023). Related work in bedrock likewise emphasizes water transport from warmer regions toward colder ice-growth locations, driven by a thermomolecular pressure gradient arising from temperature gradients under subzero conditions (Murton et al., 2006).

Previous studies have developed mechanistic and phenomenological descriptions of ice lens formation, ranging from early experimental observations and conceptual hypotheses (Taber, 1929, 1930) to modern thermomechanical frameworks that model frozen fringe processes (Rempel et al., 2004; Rempel, 2007; Meyer et al., 2023). Thermo–hydro–mechanical (THM) numerical models (Figure 7) have also been developed, compared against experimental data, to simulate ice-lens development and associated heave (Thomas et al., 2009). These detailed THM frameworks explicitly capture the couplings (Figure 7) that must be parameterized in large-scale applications.

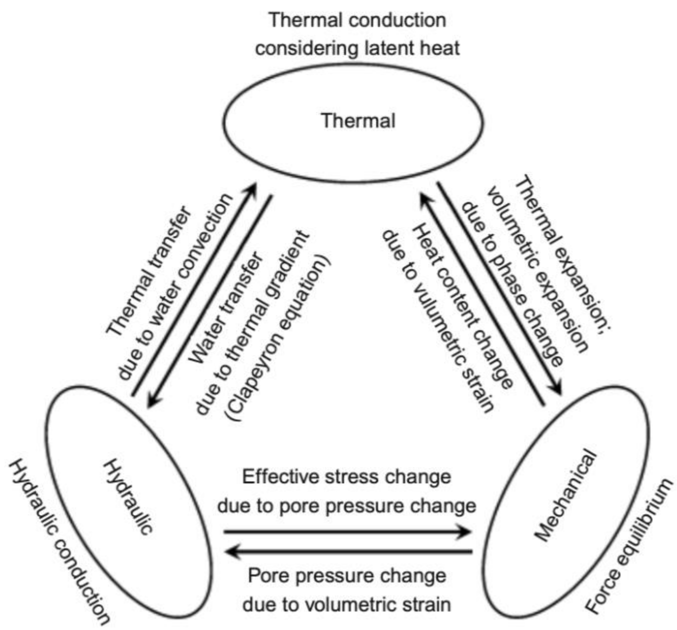

Figure 7. Thermo–Hydro–Mechanical Coupling in Freezing Soils.
Diagram illustrating the thermo-hydro-mechanical interaction mechanism in freezing soils (Reproduced from Thomas et al. 2009, Fig. 1)

Building on these frameworks, fully coupled thermo–hydro–mechanical models and multiphase-field simulations have been developed to simulate the detailed spatial evolution of ice lenses during freeze–thaw cycles, including lens initiation, growth, and subsequent thaw (melting) under transient thermal forcing. An example of such a simulation is shown in Figures 8 & 9, illustrating the formation and subsequent melting of multiple ice lenses alongside the coupled evolution of displacement, cryo-suction, temperature, and ice saturation. While these models capture a high level of physical detail, their computational expense limits their applicability at temporal and spatial scales relevant to large-scale permafrost modeling. Importantly, the qualitative behaviors observed in these high-resolution simulations, such as cyclic ice lens formation, water redistribution within the frozen fringe, and response to the imposed time-dependent thermal boundary, are consistent with the key processes reproduced by the lens-resolving framework adopted in this study (Suh and Sun, 2022). This qualitative agreement motivates the use of a simplified, physically grounded approach that retains essential frozen-fringe physics while enabling scalable analysis of ice segregation efficiency.

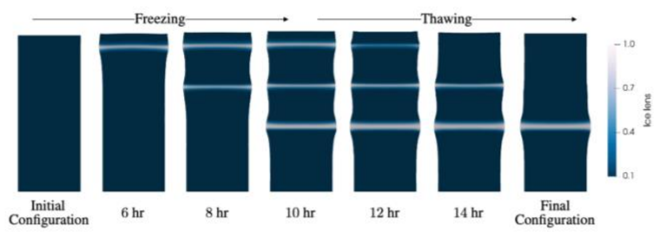

Figure 8. Ice Lens Evolution During Freeze–Thaw.
Temporal evolution of ice lens formation and subsequent melting during a numerical freeze–thaw cycle. The sequence illustrates the initiation, growth, and disappearance of multiple ice lenses under imposed freezing and thawing conditions (Reproduced from Suh & Sun (2022), Fig. 12A).

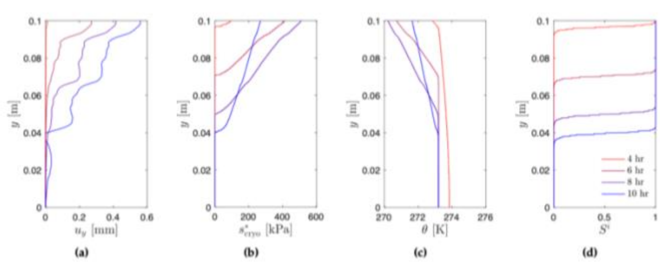

Figure 9. Coupled THM Response During Ice Lens Growth.
Coupled thermo–hydro–mechanical response of the specimen during the freezing phase. Profiles along the central axis show (a) vertical displacement, (b) cryo-suction pressure, (c) temperature, and (d) ice saturation at selected times, illustrating the co-evolution of deformation, thermal forcing, and phase change during ice lens growth (Reproduced from Suh & Sun (2022), Fig. 13).

At the microscale underlying these processes, this cryo-suction process is physically enabled by the persistence of thin unfrozen water films, even at temperatures below 0°C. These films, often only nanometers thick, remain unfrozen due to interfacial pre-melting and intermolecular forces

(Dash et al., 2006). They coat soil particles and facilitate film-water migration within the frozen fringe, providing pathways for water transport toward growing ice lenses (Fu et al., 2022). Consequently, as ice lenses grow, they alter pore structure, redistribute water, and modify the local thermal regime. These coupled thermal and hydraulic processes regulate freezing and thawing and strongly influence surface deformation and active layer thickness (Taber, 1929, 1930; Chen et al., 2020b).

The processes within the frozen fringe result in open-system frost heave, in contrast to closed-system freezing assumptions, which assume that all ice formation results solely from the freezing of local pore water with no external water supply. Quasi-static models demonstrate that sustained water migration through the frozen fringe can result in continued ice-lens growth (and frost heave) under slowly varying thermal conditions, including after the active zone reaches thermal steady state, reinforcing the fundamentally open-system nature of frost heave (Ji et al., 2019). Complementing these models, laboratory experiments have visually captured this process, showing ice-lens development, while heave and water-intake measurements indicate pore-water expulsion during in situ freezing and associated water redistribution that can supply segregation freezing (ice-lens growth) within the frozen fringe (Akagawa, 1988).

The Circumpolar Active Layer Monitoring (CALM) program (Figure 10) is a vital long-term monitoring network (Brown et al., 2000). Its field observations also confirm that ground deformation during freeze-thaw cycles often involves substantial water redistribution and ice segregation rather than pore ice freezing which refers to the solely in-situ phase changes (Nelson et al., 2021).

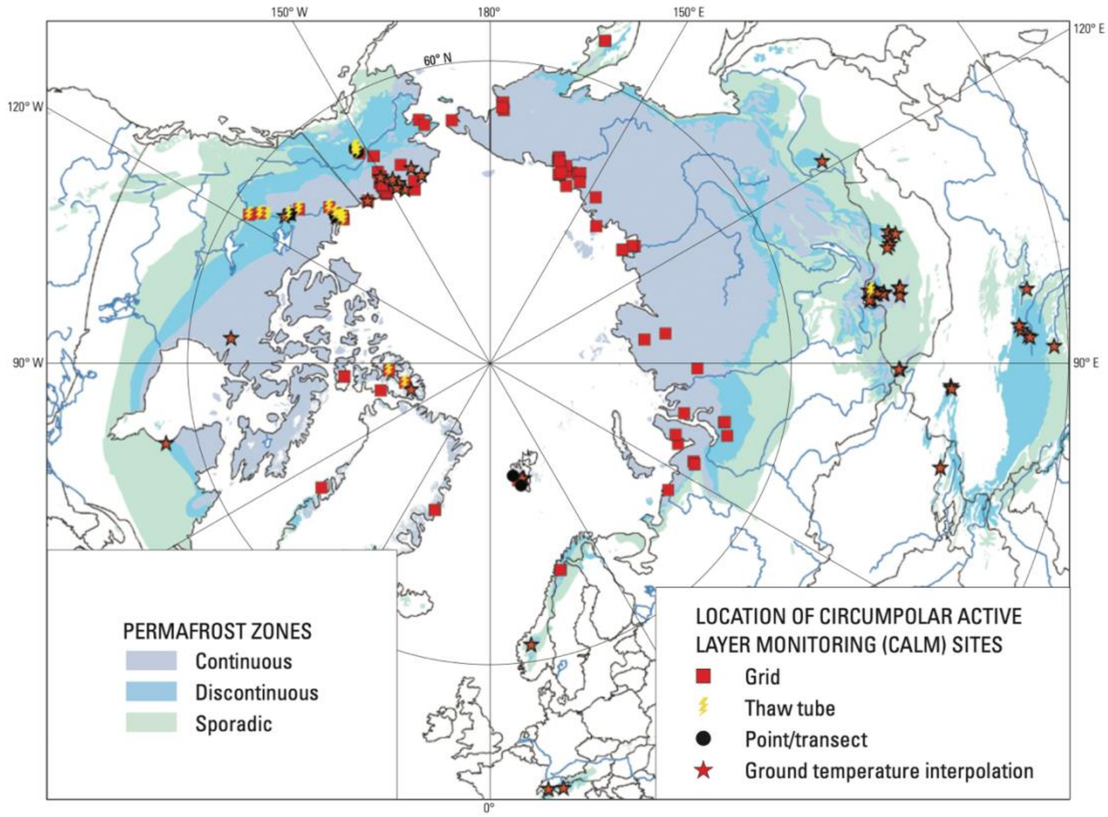

Figure 10. Permafrost Zones and CALM Monitoring Sites.
Map showing the distribution of permafrost zones (continuous, discontinuous, and sporadic) in the Northern Hemisphere, with marked locations of Circumpolar Active Layer Monitoring (CALM).

These findings underscore the complexity of predicting ice lens distribution, which arises from nonlinear interactions among soil properties, heat transfer, and stress conditions and requires integrating both thermal and hydraulic effects. Consequently, the limited representation of water migration and ice formation processes in existing models likely contributes to increased uncertainty in simulated soil water content and temperature, which may result in inaccuracies in evaluating the ecological and hydrological impacts of permafrost at the landscape scale (Fu et al., 2022).

Building on this understanding, recent advances, such as Peppin's (2022) validation of Arakawa's (1966) phenomenological model, link lens growth to thermal gradients and pore-scale forces. The microphysical foundation for these forces, based on interfacial premelting and thermomolecular interactions, has been formalized developed and incorporated into continuum frost heave models

(Rempel, 2011; Rempel et al., 2004). These models often employ a simplified freezing isotherm approach, in which the distributed frozen fringe is collapsed onto an approximate freezing isotherm. Figure 11 illustrates this simplified freezing-isotherm concept, comparing the formation of ice lenses in freezing soil with and without a frozen fringe. By collapsing the distributed frozen fringe into an effective freezing isotherm, such approaches enable simplified representations of frost heave dynamics but sacrifice spatial resolution of internal fringe processes.

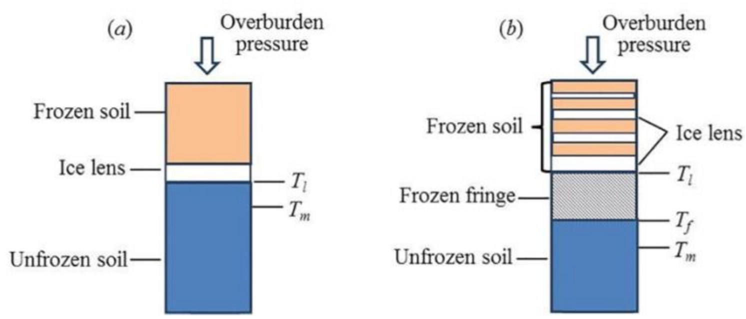

Figure 11. Ice Lens Formation With and Without a Frozen Fringe.
Schematic of ice lens formation in freezing soil, showing (a) without and (b) with a frozen fringe, providing a visual representation of how the frozen fringe influences lens growth and soil behavior during frost heave. T_m *(bulk water freezing point),* T_f *(freezing front), and* T_i *(warmest ice lens boundary). (Reproduced from Zhou & Wei (2020), Fig. 1)*

A crucial parameter in such simplified frameworks is the segregation efficiency (E) to quantify how the conductive heat flux is partitioned between advancing the freezing front and driving segregated ice growth (Arakawa, 1966). Segregation efficiency represents the fraction of total heat flux that is effectively converted into latent heat associated with ice lens formation. Values of E range from zero, corresponding to non-frost-susceptible freezing dominated by pore ice formation, to values approaching one, indicating near-complete ice segregation. This approach to parameterizing ice segregation builds upon earlier field-based concepts such as the segregation potential (SP), an empirical parameter that relates water intake flux linearly to the temperature gradient in the frozen fringe. This work established that SP is not a constant but varies with the suction at the freezing front, highlighting the need for a more fundamental, process-based parameter (Konrad and Morgenstern, 1981).

Although SP has proven useful for engineering predictions and validated against field data (Fukuda and Kinosita, 1985), its empirical nature limits its generalizability across diverse conditions. This thesis seeks to derive a thermodynamically constrained analog, segregation efficiency (E), from first principles, moving beyond an empirical constant toward a variable efficiency emergent from coupled microscale processes.

Despite their utility, existing parameterizations of segregated-ice formation remain limited in their ability to capture the evolving thermomechanical structure of the frozen fringe. Ice saturation, permeability, and effective stress vary spatially and temporally within this zone, exerting strong controls on water supply and lens growth. Moreover, the microscale assumptions in rigid-ice models, particularly regarding heave rates and ice lens initiation, are not yet fully established (Fu et al., 2022), which may affect model robustness across different physical conditions. While foundational analytical work exists on discrete ice lens formation (Nixon, 1991), fully resolving these processes remains computationally intensive and difficult to implement in large-scale permafrost models (Smith, 2022). Consequently, there is a critical need for physically grounded approaches that retain essential microscale physics while producing scalable metrics suitable for regional and continental modeling frameworks, following successful precedents of subgrid parameterizations of heterogeneous land-surface processes (e.g., Aas et al., 2019) and, in data-driven settings, by augmenting training datasets with synthetic data generated by physics-based hydrodynamic simulations, which has been shown to improve machine learning predictive skill in hydrology, particularly for high-flow conditions (López-Chacón et al., 2023).

At larger spatial scales, however, permafrost models typically rely on simplified representations of ice segregation or neglect it altogether. While segregation efficiency has been proposed as a means of bridging this gap (Arakawa, 1966; Peppin, 2022), its dependence on evolving thermal, hydraulic, and mechanical conditions appears to remain poorly constrained. While state-of-the-art community models like CryoGrid have begun to incorporate ice segregation schemes to simulate long-term landscape evolution (Aga et al., 2023), these models still require more robust, physically derived parameterizations of the frozen fringe. By refining the mechanical constraints on ice lens growth (Stubblefield, 2025), this thesis aims to provide the necessary thermodynamic bounds to improve these large-scale simulations.

This thesis addresses this gap by using a lens-resolving frost heave model to investigate how segregation efficiency depends on thermal forcing, sediment properties, and stress conditions within the frozen fringe. Specifically, this work asks: (1) how sediment properties (porosity φ, ice saturation S_s, permeability k) and thermal gradients influence segregation efficiency in porous media; (2) how effective stress and surface heat flux regulate ice lens formation and the conditions under which they promote or suppress segregated ice growth; and (3) to what extent a lens-resolving frost heave model can capture the temporal evolution of segregation efficiency under varying thermal and sediment conditions, and what limitations arise under idealized assumptions. The model explicitly represents spatial variations in ice saturation and permeability, while resolving heat flux partitioning across the freezing zone, allowing segregation efficiency to be computed dynamically from local energy and mass balances.

By incorporating geothermal heat flux and mechanical loading via an effective-stress work seeks to link microscale ice lens growth processes to macroscale predictions of frost heave and active layer dynamics. In doing so, the thesis evaluates the extent to which segregation efficiency can serve as a physically constrained, scalable parameter for improving large-scale permafrost simulations.

II. METHOD

2.1. Overview of the Modeling Framework

To bridge the scale between pore-scale processes and landscape dynamics, this study employs a one-dimensional lens-resolving frost heave model that resolves the formation and growth of individual ice lenses, enabling detailed simulation of vertical processes while maintaining computational tractability. This approach is chosen to investigate the physical controls, such as thermal gradients, permeability, and effective stress (Rempel, 2011), on the initiation and growth of a new lens within the frozen fringe, which is essential for quantifying segregation efficiency (E). The modeling framework utilizes an idealized porous medium consisting of inert sediment and pure water to focus on core processes. By excluding the complexities of sediment heterogeneity and chemical solutes, the model isolates the primary thermodynamic, hydraulic, and mechanical (THM) interactions, ensuring consistency with baseline conditions from experimental studies of confined freezing. Our model explicitly resolves spatial variations in temperature, ice saturation, permeability, and stress within the frozen fringe, enabling segregation efficiency to be computed dynamically from local energy and mass balances via coupled equations.

Thermal forcing is imposed through prescribed heat-flux boundary conditions: an imposed surface heat flux Q_s (0.06–100 W/m²) and a basal geothermal heat flux $Q_g = 0.06$ W/m². The resulting temperature field is computed internally by the model. Sediment properties (porosity and permeability) and overburden pressure (64-75 kPa) are specified to isolate their influence on ice segregation dynamics.

2.2. Theoretical Framework: Ice Lens Nucleation and Cyclical Growth

Our model is built upon the coupled conservation laws of energy, mass, and momentum, which govern ice lens formation in freezing soils by integrating thermal, hydraulic, and mechanical processes (Rempel et al., 2004). The following subsections outline the specific constitutive relationships and criteria used within this framework. In this framework, ice lens growth arises from the interaction between thermal gradients, water migration, and mechanical loading within the frozen fringe. The following subsections outline the governing relationships used to characterize these processes and to identify the conditions under which ice lenses nucleate, grow, and terminate. These coupled processes are illustrated conceptually in Fig. 12.

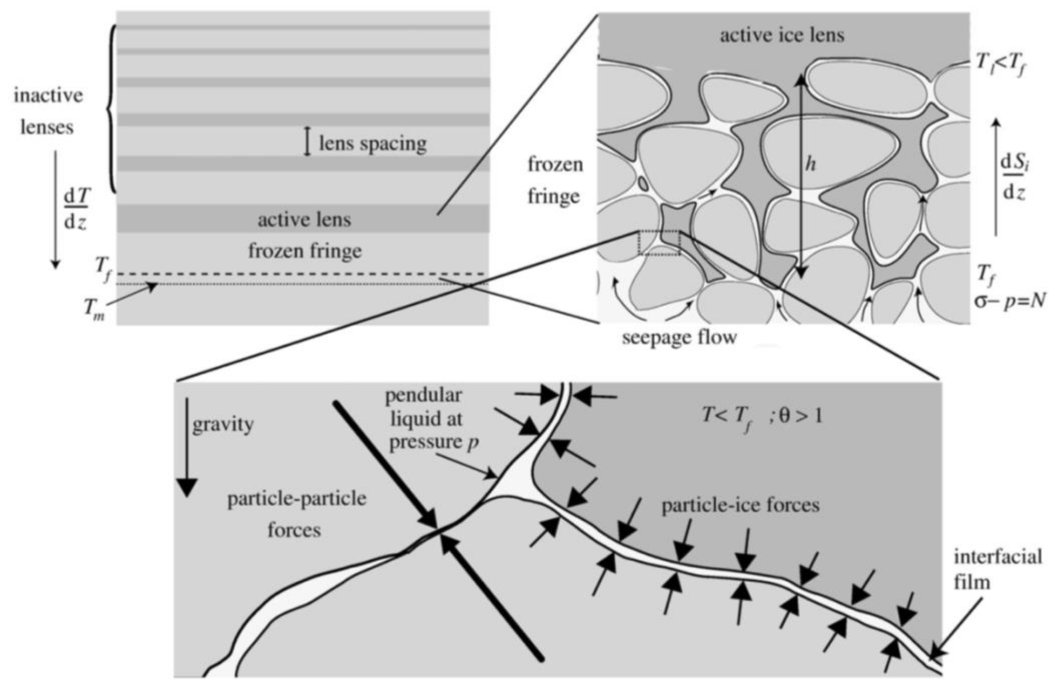

Figure 12. Coupled Processes in Ice Lens Formation.
Schematic of the coupled processes governing ice lens formation within the frozen fringe. As temperature decreases with depth (z) below the melting front (T_m), ice saturation (S_i) increases, creating a partially frozen zone (the frozen fringe) where water migration and lens growth occur under a balance of thermodynamic and mechanical forces (Reproduced from Rempel, 2011).

2.2.1. Energy balance (Thermodynamic Equilibrium: Clausius–Clapeyron equation)

The thermodynamic driving force for ice lens formation is captured by the Clausius–Clapeyron relation, which links temperature depression below the bulk melting temperature to the pressure difference between ice and liquid water. Assuming local thermodynamic equilibrium at the ice–water interface and neglecting solute effects and interfacial curvature/disjoining-pressure contributions, the linearized Clausius–Clapeyron relation gives the required ice–water pressure difference associated with an undercooling $T_m - T$:

$$P_i - P_w = \rho_w \ L \frac{T_m - T}{T_m} \quad (1)$$

As T decreases below T_m, the equilibrium requires a larger $P_i - P_w$. In freezing soils, P_i is typically constrained by the local mechanical loading/effective stress state, so the increase $P_i - P_w$ manifests primarily as a decrease in pore-water pressure (more negative P_w), producing cryo-suction that draws unfrozen water toward colder regions, facilitating ice lens formation (Rempel et al., 2004; Dash et al., 2006; Yu et al., 2024). This relation provides a direct correspondence between thermal gradients and mechanical forces and allows the force balance governing lens formation to be expressed equivalently in pressure or temperature space. This equivalence is utilized in both discrete lens models (Nixon, 1991) and contemporary phase-field formulations (Suh and Sun, 2022). Throughout this study, temperature depression is used as the primary measure of the thermodynamic driving force. Although the application of the Clapeyron relation under dynamic conditions is an area of ongoing discussion (e.g., Fu et al., 2022), and its validity within the transporting frozen fringe has been questioned (Konrad and Morgenstern, 1981), it provides a fundamental thermodynamic basis for the cryo-suction driving force in this study, justified by the quasi-static nature of simulated processes for slow permafrost freezing rates. This formulation, which links temperature depression to a suction pressure, provides the fundamental thermodynamic driving force for water migration in freezing soils and is consistently employed in modern coupled THM models of permafrost behavior (e.g., Liew & Xiao, 2022). The pressure difference ($P_i - P_w$) defines the cryo-suction potential that drives water flow according to Darcy's

Law (Section 3.2.2). More generally, curvature (capillarity or Gibbs–Thomson), solutes, and disjoining pressure can modify the equilibrium condition; here Eq. (1) isolates the dominant thermal contribution used to define a macroscopic cryo-suction driving potential,

2.2.2. Mass conservation (for Water Migration)

The supply of water to growing ice lenses is governed by mass conservation principles applied to liquid water within the partially frozen pore space of the frozen fringe. Changes in liquid water content reflect the divergence of water flux within the frozen fringe, which is modeled using Darcy's law under frozen-soil conditions. Although the presence of ice reduces pore connectivity, unfrozen water can remain hydraulically connected over a narrow subzero interval near 0 °C (e.g., ~0 to −4 °C in fine clay, ~0 to −0.2 °C in coarser materials, and ~0 to −0.7 °C in Devon silt; Kjelstrup & Ghoreishian Amiri, 2021), permitting hydraulic transport toward the freezing front. Permeability in the frozen fringe is commonly parameterized as a strong decreasing function of ice saturation (often using power-law forms), so that increasing ice saturation progressively reduces water flow (Rempel, 2007; Meyer et al., 2023). This frozen-fringe permeability reduction is often linked to the decline in effective porosity (or unfrozen water content), which Kozeny–Carman-type relations provide a basis for permeability estimation in unfrozen soils (Ji et al., 2019). In advanced THM formulations for freezing soils, hydraulic conductivity is commonly expressed using a relative-permeability function of liquid (or ice) saturation and an absolute permeability relation that depends on porosity (Yu et al., 2024). Since saturation and porosity-dependent permeability control the Darcy flux q, the evolution of liquid water content in the frozen fringe is obtained by applying mass conservation to that flux. Thus, mass conservation is expressed as:

$$\frac{\partial \phi_l}{\partial t} - \nabla . \mathrm{q} = 0 \qquad (2)$$

where $\partial \phi_l / \partial \mathrm{t}$ is the time rate of change of liquid volumetric content (units: 1/s)

The water flux $\nabla.q$ is driven by the cryo-suction gradient via Darcy's law:

$$q = -\frac{k}{\mu}\nabla P_w \qquad (3)$$

Where k is the ice-saturation-dependent permeability.

This formulation captures the competition between cryo-suction–driven water migration and permeability loss due to freezing. This equation states that the change in liquid water content over time equals the net flow of water into that region. Darcy’s law governs flow, indicating that water always flows from high pressure to low pressure, with the ease of movement depending on the permeability (k) and viscosity (μ).

2.2.3. Momentum balance (Mechanical Equilibrium)

Ice lens formation requires that upward forces generated by thermodynamic and hydraulic processes overcome the downward effective overburden stress imposed by the weight of the overlying soil and ice. In a one-dimensional vertical framework, mechanical equilibrium is achieved when ice pressure, disjoining (thermomolecular) pressure, and hydraulic forces (pore water pressure) collectively balance the applied load (Rempel et al., 2004; Fu et al., 2022). When this balance is disrupted such that the resisting contact stress vanishes, a new ice lens can nucleate. This force balance provides the mechanical criterion for ice lens initiation and explains the cyclical nature of frost heave (Meyer et al., 2023).

The total overburden stress σ_n is partitioned between pore water pressure P_w and the effective stress N carried by the soil skeleton:

$$\sigma_n = N + P_w \qquad (4)$$

Disjoining (thermomolecular) Π pressure across the premelted film at the ice–solid water interface, under local equilibrium equals to the ice–water pressure difference.

$$P_i - P_w = \Pi \quad (5)$$

Ice lens nucleation occurs when the interparticle contact stress vanishes:

$$N = 0 \quad (6)$$

Where N = Effective stress supported by the soil skeleton (grain–grain contacts).

Combining Eqs. (4) and (5) show how the applied load is transmitted through pore water and thermomolecular stresses to the ice lens. So, from (4) and (5) at N = 0:

$$P_i = \sigma_n + \Pi \quad (7)$$

Given the idealized homogeneous media considered here, we employ the effective-stress criterion (Eq. 6), which, together with the stress partition (Eq. 4) and interface relation (Eq. 5), captures the net resistance to lens initiation. Our model uses the fundamental force balance but acknowledges that this additional micro-mechanical threshold can influence precise nucleation temperatures.

2.2.4. Force Balance in Temperature Coordinates

To couple the mechanical initiation criterion with the thermodynamic state, we rewrite the ice–water pressure difference in terms of temperature depression $\Delta T = T_m - T$. Under local thermodynamic equilibrium at the ice–water interface and neglecting solute and curvature effects, the linearized generalized Clapeyron relation gives a direct proportionality between undercooling (temperature depression) and the ice–water pressure difference:

$$P_i - P_w = \rho_w L \frac{T_m - T}{T_m} \quad (8)$$

In section 3.2.3. we defined the thermomolecular disjoining pressure Π across premelted films by the interface relation:

$$P_i - P_w = \Pi$$

so, combining Eq. (5) with Eq. (9) yields a thermal coordinate expression for the thermomolecular driving stress:

$$\Pi = \rho_w L \frac{\Delta T}{T_m} \quad (9)$$

At lens nucleation, the interparticle contact stress vanishes (Eq. 6), and using the stress partition $\sigma_n = N + P_w$ (Eq. 4) implies $P_w = \sigma_n$. Therefore, the ice pressure at initiation can be written as

$$P_i = P_w + \Pi = \sigma_n + \Pi = \sigma_n + \rho_w L \frac{\Delta T}{T_m} \quad (10)$$

Mapping the force balance onto thermal coordinates allows the thermodynamic driving force for segregation to be quantified directly from the temperature field, simplifying the analysis of lens nucleation conditions.

2.2.5. Cyclical Lens Nucleation, Growth, and Termination

Using the initiation criterion developed in sections 3.2.3–3.2.4 (expressed either in pressure form or in thermal coordinates), our model represents lensing as a repeated sequence of nucleation, growth, and termination. The cycle begins when, near the warm boundary of the frozen fringe (temperatures just below T_m), the relatively high permeability enables efficient water supply. Here, if the combined thermodynamic (cryosuction / Clapeyron) and interfacial (disjoining) effects overcome the overburden resistance (Eq. 4-6), a new lens nucleates. As the freezing front advances and the local temperature at the lens boundary decreases, ice saturation increases in the underlying fringe. This reduces the porosity available for water flow, consequently lowering permeability, limiting the water supply, and thereby decelerating lens growth. Growth continues until permeability becomes sufficiently reduced that the water supply cannot sustain further growth, defining a termination threshold $T_{\max}$. The system then nucleates a new lens at a warmer position, repeating the cycle (Rempel, 2007). This study adopts a quasi-static approach (Ji et al., 2019), treating lens evolution as a sequence of equilibrium states. The transitions between cycle stages are tracked within the model using three key diagnostic temperatures, T_{first}, T_{new}, T_{max}, and the heaving capacity (H_c), as derived below:

First temperature at which a lens can exist: T_{first}

The temperature T_{first} defines the thermodynamic-mechanical threshold at which a discrete ice lens can first become mechanically stable within the frozen fringe. It represents the point where the cryosuction pressure generated by thermomolecular (disjoining) forces is precisely balanced by the overburden pressure, under the assumption of no net water flow, a hydrostatic equilibrium condition (an idealization, real fringes have minimal flow at onset). Following the (Rempel, 2007) approximate criterion, T_{first} is obtained by balancing thermomolecular forcing against the integrated mechanical support of the partially ice-saturated fringe and the applied overburden written in temperature coordinates via the Clapeyron scaling. Each term has the units of temperature (K):

$$\left(T_m - T_{first}\right)\emptyset S(T_{first}) - \int_{T_{first}}^{T_f} \emptyset S(T)dT - \frac{P_0 T_m}{\rho_i L} = 0 \qquad (11)$$

$\left(T_m - T_{first}\right)\emptyset S$: This term is the local undercooling at the lens boundary, weighted by the local pore-ice fraction. When multiplied by the Clapeyron scaling $(\rho_i L/T_m)$, it corresponds to the local thermodynamic driving stress available to support lens initiation.

$\int_{T_{first}}^{T_f} \emptyset S(T)dT$: Each small temperature interval between T_{first} and T_f has some partially frozen pores that already support part of the overburden. This accounts for the cumulative integrated partial support of the overburden by the ice-saturated sediment matrix across the frozen fringe between T_{first} and the fringe top T_f.

$\frac{P_0 T_m}{\rho_i L}$: Converts the applied overburden stress P_0(Pa) into an equivalent undercooling (K) using Clapeyron scaling.

Initially, the fringe is thin and has high permeability, facilitating water movement. T_{first} marks where the upward suction force caused by freezing is strong enough to balance the weight of the soil above it, but the lens has not yet started growing. The equation at this stage represents the force balance when a lens is just barely possible (no water flow yet).

- Nucleation Stage:

A new ice lens initiates at a relatively warm temperature T_{new} where the frozen fringe is thin, and permeability is high. This allows rapid initial growth V_{new}, as thermodynamic driving is strong. The governing equation at this stage is built on the same force balance, but now incorporates water flow resistance, thereby permitting lens growth. By combining these driving and resisting terms, the force balance yields an expression that is called critical heaving capacity $H_c(T)$. In practice, T_{new} corresponds to the location in the fringe where H_c is maximal (the mechanically weakest point). A new lens initiates when this condition is met simultaneously with the evolving lens state (which is the intersection/zero-contact-stress criterion in Rempel, 2007). Thus, the lens nucleates at the temperature where $H_c(T)$ is largest (Rempel, 2007).

Here $H_c(T)$ is evaluated as a function of the temperature coordinate T through the fringe, and T_{new} is the value of T that maximizes H_c.

$$H_c(T) = \frac{(T_m - T)\emptyset S - \int_T^{T_f} \emptyset S dT - \frac{P_0 T_m}{\rho_i L}}{\int_T^{T_f} (1 - \emptyset S)^2 / K) dT} \qquad (12)$$

H_c: critical heaving capacity (m^2, scaled proxy form)

Here we use a scaled critical heaving-capacity proxy (driving/resistance ratio) consistent with the implementation in our code; the full dimensional prefactor in Rempel (2007) can be reinstated if absolute rates are needed.

$\int_{T}^{T_f}(1-\emptyset S)^2/K)dT$: The denominator represents the integrated hydraulic impedance of the frozen fringe (cumulative flow resistance as permeability decreases with increasing ice saturation). In practice, $k(T)$ is parameterized as a strong decreasing function of ice saturation (or unfrozen water fraction), using Kozeny–Carman-type (Chen et al., 2021) or relative-permeability forms (Rempel, 2007).

$1-\emptyset$S: a proxy for the reduction in connected flow pathways / available flow area as pore ice accumulates.

The numerator represents the net driving for lens growth expressed in temperature coordinates (undercooling/disjoining contributions minus the Clapeyron-scaled overburden), while the denominator represents the flow resistance through the frozen fringe.

Indeed, as temperatures decrease slightly (colder than T_{first} within the fringe), suction strengthens, but permeability begins to drop due to more frozen pores. There is a specific condition in which the temperature is sufficiently low to create strong suction, but the pores remain open enough for easy water flow. The temperature under this condition is T_{new} , the actual temperature where a new lens nucleates and begins to grow. Under this condition, cryo-suction is strong and permeability is still high (due to a thin fringe), resulting in a large initial V_{new} growth rate.

The force balance governing ice lens growth (Eq.13) accounts for the integrated hydraulic resistance of the frozen fringe through the permeability term $\int(1-\phi S)^2/K\,dT$ (Rempel, 2007). This formulation represents the macroscopic effect of interfacial hydraulic resistance, the resistance to flow within the premelted film between the ice lens and sediment grains, which is an important control on heave rates when the frozen fringe is thin. As visualized in Figure 13, this resistance emerges at the grain scale from viscous flow in thin premelted unfrozen water films separating ice from sediment grains (Zhou & Wei, 2020).

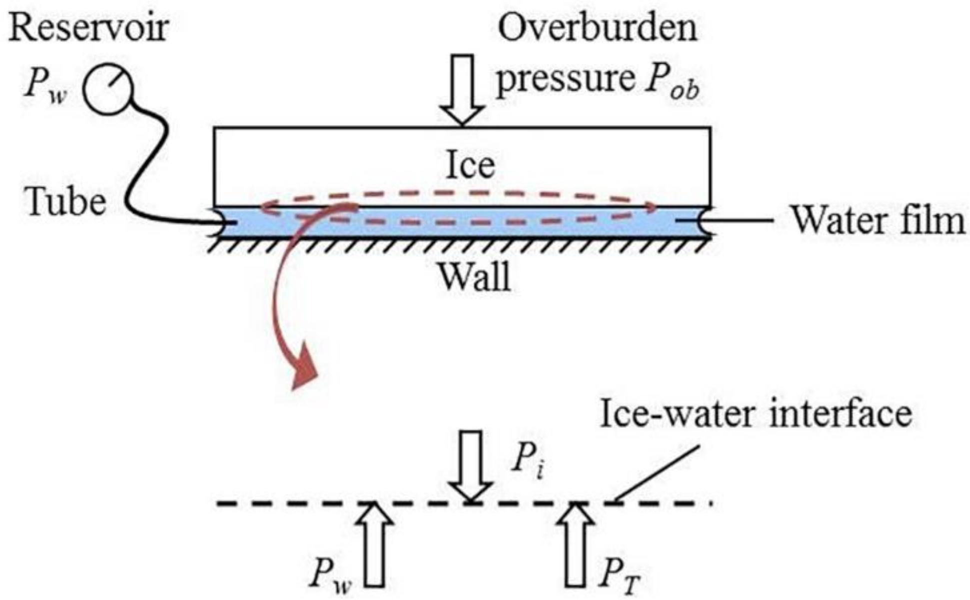

Figure 13. Interfacial Water Films and Hydraulic Resistance.
Conceptual depiction of grain-scale interfacial hydraulic resistance at the ice-lens/solid-substrate (grain) interface. This resistance originates in thin premelted (unfrozen) water films between ice and the solid substrate, where related pressures (e.g., disjoining and normal stresses) influence flow (redrawn from Zhou & Wei, 2020, their Fig. 4). This effect can become important when the frozen fringe is thin. Π *(our notation) corresponds to* P_T *in Zhou & Wei (2020).*

Drawing from the interfacial dynamics illustrated in Figure 13, our approach represents the combined effect of fringe and interfacial resistance through an effective temperature-dependent permeability $k(T)$, which effectively homogenizes the combined effects of fringe and interfacial flow resistance into a single, tractable parameter. This simplification is appropriate here because our analysis focuses on how fringe thickness and permeability evolution regulate water supply, rather than explicitly resolving grain-scale film flow (Rempel, 2007; Zhou et al., 2020). Thus, our integrated permeability approach provides a computationally efficient approximation of the more detailed interfacial physics, suitable for exploring the parameter space of segregation efficiency.

- Growth Deceleration: As the freezing front advances downward, the frozen fringe thickens, and temperatures within the frozen fringe beneath the lens decrease further below the melting point.

Ice clogging reduces permeability, thereby restricting water supply and decreasing ice lens growth rate (and thus heave rate) as evidenced by the time evolution of the heave curves in Figure 14.

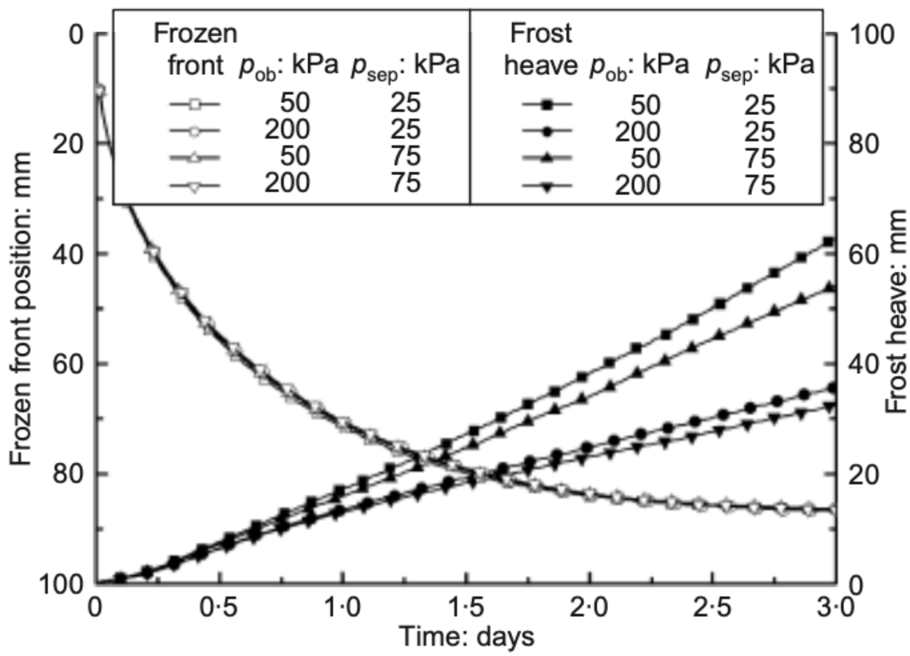

Figure 14. Frozen Front Advancement and Frost Heave Evolution.
Evolution of frozen front position (left axis) and frost heave (right axis) over time for typical one-sided freezing conditions under varying overburden pressures (P_{ob}) and separation pressures (P_{sep}), demonstrating growth deceleration (reproduced from Thomas et al., 2009).

Figure 14 supports our model's treatment of fringe thickening as the primary deceleration mechanism. This deceleration manifests as reduced heave rates over time, directly influencing the average growth velocity used in our segregation efficiency calculations.

- Termination and Renewal: Growth slows until a critical threshold undercooling temperature (T_{max}) is reached, at which the lens growth rate reaches a minimum (Vmax). At this point, cryo-suction can no longer sustain water flux, triggering nucleation of a new lens at a shallower, warmer depth (T_{new}), and restarting the cycle (Rempel, 2007).

$$H_c(T_{new}) = H(T_l) = \frac{T_m - T_l - \int_{T_l}^{T_f} \emptyset S dT - \frac{P_0 T_m}{\rho_i L}}{\int_{T}^{T_f} (1-\emptyset S)^2 / K) dT} \quad (13)$$

The solution to this equation is where the lens temperature (T_l) is equal to (T_{max}).

Indeed, within the frozen fringe below the lens, critical heaving capacity H_c indicates how close a given level (temperature T) is to losing interparticle contact support; a new lens can initiate when heaving capacity H becomes large enough to becomes equal to the critical heaving capacity H_c of the existing lens.

Because $H_c(T, T_l)$ varies across the fringe, the first temperature T_{new} at which a new lens can form is where H_c is maximal (this is the "weakest" point in the fringe). The condition $H_c(T_{\text{new}}, T_l) = H(T_l)$ therefore defines the moment when the particle contacts at another point (corresponding T_l) can no longer bear load and a new lens is triggered. Rempel, (2007) labels this threshold as the "max" point ($T_l = T_{\max}$), after which a new lens forms at a warmer temperature below ("new").

From the average of the gradients at the fringe top and fringe bottom, we can find a representative fringe temperature gradient based on Fourier's law. Using a 1-D energy balance and Fourier's law for conduction, we estimate a representative frozen-fringe temperature gradient as:

$$\frac{T_f - T_l}{Z_f - Z_l} \cong \frac{1}{2}\left[\frac{Q_s + Q_g}{K_T} - \frac{\rho_i L}{K_T}(1 - \emptyset S_{zl})V\right] \qquad (14)$$

Eq.14 (permeability) belongs to the Darcy fluid-flow part of the model: water delivery toward the lens is described by Darcy's law, with an effective permeability that decreases as ice saturation increases. Because ice saturation is prescribed as a function of temperature $S_s(T)$, permeability can also be treated as temperature-dependent, $k(T)$.

Eq.15 (thermal diffusivity or thermal transport) belongs to the energy balance heat equation part of the model. Once lens growth is treated as a transient freezing (Stefan) problem, the temperature field must evolve in time, and this requires a parameter controlling how quickly temperature gradients adjust (thermal diffusivity κ, or equivalently thermal conductivity K_T together with specific heat capacity).

Eq.14 therefore controls how efficiently water can be supplied to the lens (hydraulic limitation via k), while Eq.15 controls how efficiently latent heat can be removed (thermal limitation via κ or K_T). Lens temperature and growth rate are governed by both mechanisms acting together.

Here, Eq.15 is an effective average thermal gradient across the fringe that includes a latent-heat sink term proportional to freezing rate (V), and then we can find the lens velocities $V_{new}$and V_{max} from Darcy flow:

$$V = \frac{\rho_w L(T_f - T_l)}{\mu T_m (Z_f - Z_l)} H \qquad (15)$$

If we combine these last two expressions, we obtain:

$$V = \frac{\rho_w L}{2\mu T_m K_T} H\big(Q_s + Q_g\big)[1 + \frac{\rho^2 l^2}{2\mu T_m K_T} H(1 - \phi S)]^{-1} \qquad (16)$$

This equation is essentially Darcy + Clapeyron mapping, with H acting as the “integrated hydraulic conductance/resistance” lumped term.

Approximate the average lens velocity as:

$$\bar{V} = \frac{V_{new} + V_{max}}{2} \qquad (17)$$

Although the frozen fringe is a zone of coupled phase change and flow, the temperature profile across it can be reasonably approximated as linear for modeling purposes, a simplification validated by comparative numerical studies (Nixon, 1991; see Fig. 15 adapted from Nixon’s Fig. 5). This allows the use of analytical heat balance equations while retaining essential physics.

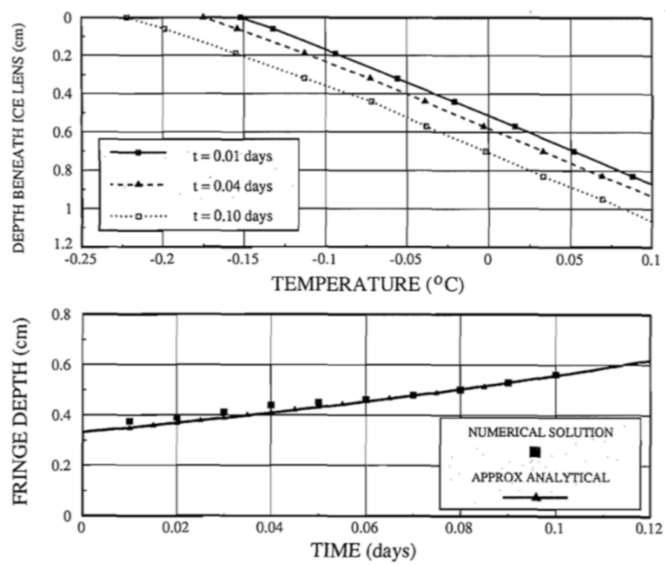

Figure 15. Linear Temperature Profile in the Frozen Fringe.
Numerical validation of the assumption of a linear temperature profile in the frozen fringe. Parameters include a sample base temperature of +2.7°C, a cooling rate of 0.84°C/day, a sample height of 10 cm, an initial lens temperature of -0.14°C, constants A = 0.05 and B = 0.5, a water content W = 20%, and an initial freezing point of -0.04°C. Note that this simulation is limited to temperature profiles during the formation of a single ice lens (Adapted from Nixon (1991), Fig. 5)

2.3. Modeling Approach: Bridging Process Dynamics and Efficiency

Arakawa (1966) simplified ice lens growth by collapsing the frozen fringe into a single freezing isotherm, defining segregation efficiency (E); here we express Arakawa's definition in an equivalent form:

$$E = \frac{\rho_i L V}{q_{heat}} \qquad (18)$$

This work builds on Arakawa's framework by advancing the role E as a key parameter. Instead of collapsing the fringe to an isotherm, we incorporate its thermomechanical complexity, considering it as a thermal gradient zone. We account for temperature-dependent ice saturation S(T), permeability variations k(S), and effective stress (N), building on Rempel's (2007) framework, to model how ice lenses nucleate and grow within the fringe. Our proposed approach differs from land-surface permafrost modeling frameworks that simulate ice segregation and associated heave/subsidence using soil-mechanics concepts (effective stress, compressibility) rather than explicitly resolving thermomolecular (disjoining) forces at ice–sediment interfaces (Aga et al., 2023; Rempel, 2007).

2.4. Parameterization of Ice Saturation and Permeability

The permeability and ice saturation are modeled as non-linear functions of temperature. This power-law formulation is widely used in frost heave modeling and effectively captures the essential sealing of permeability and increase in ice saturation with temperature depression within the frozen fringe (Rempel, 2007, 2011). These relationships draw on empirical and theoretical foundations: Devoie et al. (2022) compiled a large database of empirical soil freezing characteristic curves describing how ice saturation S varies with temperature T, while Chen et al. (2020a) developed a straightforward procedure for calculating S(T) for clastic sediments with specified particle-size distributions. Calculations by Chen et al. (2021) support a modified Kozeny–Carman formula that aligns with experimental data and has been successfully employed in discrete ice lens models to predict heave rates and lens spacing (Nixon, 1991; see Fig. 2 for data compilation).

Similar empirical power-law relationships linking ice saturation and permeability to temperature depression have been successfully employed in coupled THM models of frost heave, supporting their utility in capturing essential frozen fringe dynamics (Thomas et al., 2009, Fig. 3; Eq. 4). The equations link ice segregation dynamics to measurable sediment properties (e.g., particle size) and environmental conditions (temperature), enabling physically realistic simulations of frost heave.

In this study, ice-lens initiation and growth are modeled using a premelting (thermomolecular/disjoining-pressure) framework, rather than an empirical Rigid Ice Model (RIM). Premelted films are not resolved explicitly; instead, their macroscopic effect is incorporated through the disjoining-pressure term in the force balance and through a saturation-dependent permeability, expressed as empirical power laws:

$$k(T) = k_0 \left(\frac{T_m - T_f}{T_m - T}\right)^{\alpha} \quad (19) \quad , \quad S(T) = 1 - \left(\frac{T_m - T_f}{T_m - T}\right)^{\beta} \quad (20)$$

Where k_0: Reference permeability (permeability at a given reference condition), T_f Freezing temperature (temperature where ice first forms in the pores), α & β: Empirical exponents controlling how permeability and saturation change with temperature.

By setting the empirical exponents $\alpha = 4$ and $\beta = 2$ the temperature scale $\Delta T_f = T_m - T_f = 0.1$°C (with reference permeability $k_0 = 10^{-15}$ m^2) following Rempel (2007, Table 1), the model prescribes how rapidly permeability seals and ice saturation increase with temperature depression within the frozen fringe. This mechanistic choice is significant because it allows the model to derive heaving capacity (H) directly from the intermolecular force balance at grain contacts, providing a physically grounded threshold for ice lens nucleation. The non-linear reduction in permeability as a function of ice saturation, which drives the hydraulic resistance in the fringe, is detailed in Appendix C. Also, more details and the corresponding derivation, adapted from Rempel (2011), underscore how power-law parameterizations yield physically constrained bounds on E under varying heat fluxes and sediment types can be found in Appendix D.

2.5. Cyclical Lens Dynamics

This study examines the dependence of lens nucleation temperatures (T_{new}, T_{max}) and growth rates (V_{new}, V_{max}) on surface heat flux (Q_s) and overburden pressure (P_o) across sediment types. This allows us to capture the interplay between heat flux, water transport, and sediment mechanics across the fringe's thermal gradient.

First, we will track the evolution of lens growth rates as the freezing front penetrates deeper and compare the associated net rate of latent heat release to the overall heat flux. Rapid initial growth V_{new} at T_{new} slows to V_{max} at T_{max} due to ice clogging and extended fringe thickness. The numerical simulations for an idealized sample scenario are conducted using an idealized one-dimensional soil column whose physical and thermal properties are summarized in Table 1(based on Rempel, 2007).

Table 1. Parameters selected to represent frost-susceptible silts.
(with values reproduced from Rempel (2007) unless noted)

Symbol	Description	Value	Units	Source / Justification
ρ_i	Ice density	920	kg m^{-3}	Standard value
ρ_l	Water density	1000	kg m^{-3}	Standard value
L	Latent heat of fusion	3.34×10^5	J kg^{-1}	Rempel (2007)
μ	Dynamic viscosity of water	1.8×10^{-3}	Pa s	At 0 °C
$\emptyset$	Porosity	0.35	–	Assumed typical sediment
k_0	Intrinsic permeability	1×10^{-15}	m^2	Rempel (2007)
ΔT_f	Freezing temperature depression	0.1	K	Assumed
T_m	Melting temperature	273	K	Constant
β	Ice saturation exponent	2	–	Rempel (2007)
α	Permeability exponent	4	–	Rempel (2007)
κ	Thermal diffusivity	0.7×10^{-6}	m^2 s^{-1}	Rempel (2007)
C	Specific heat capacity	1300	J kg^{-1} K^{-1}	Rempel (2007)

The parameter values are chosen to be representative of fine-grained, frost-susceptible soils and are adapted from the theoretical framework of Rempel (2007). Where applicable, standard thermophysical constants are employed, and selected parameters are systematically varied to investigate their impact on segregation efficiency.

The analysis focused on three key temperature thresholds derived from the model: the initiation temperature for an ice lens under hydrostatic conditions (T_{first}), the specific temperature for subsequent lens formation (T_{new}), and the upper-temperature limit (T_{max})), the maximum undercooling that a lens reaches before new lens initiation at T_{new}. These thresholds were determined by solving the force equilibrium and heat flow constraints outlined in Rempel (2007). These idealized simulations serve as a baseline for further simulations with realistic sediment and environmental conditions (Figures 17 & 18).

Second, we will assess how segregation efficiency depends on sediment properties, effective stress, and the jump in heat flux across the freezing zone (Figure 19).The concept of segregation efficiency (E) was first introduced by Arakawa (1966) as a means of quantifying the proportion of the total heat flux across a freezing front that contributes to the formation of segregated ice. Mathematically, it is expressed as

$$E \approx \frac{uL}{K_1 \frac{\partial T_1}{\partial x} - K_2 \frac{\partial T_2}{\partial x}} \quad (21)$$

where u denotes the rate of ice segregation (mass of ice formed per unit area per unit time), L is the latent heat of fusion of ice, and K_1, K_2, T_1, and T_2 represent the thermal conductivities and temperatures of frozen and unfrozen soil, respectively.

Physically, E describes the efficiency with which the total conductive heat flux is converted into latent heat associated with ice-lens growth. A value of E = 1 corresponds to perfect segregation, where all heat flux is consumed in lens formation; E = 0 represents non-frost-susceptible freezing with no segregation; and intermediate values ($0 < E < 1$) signify imperfect segregation, where part of the heat flux contributes to pore freezing rather than lens growth.

Arakawa emphasized that while the efficiency parameter was introduced partly for mathematical convenience, it also holds direct physical meaning: it captures the fraction of the total heat transfer that is effectively utilized for segregated ice growth, thereby linking heat conduction and mass transport across the freezing interface within a single unified formulation (Arakawa 1966).

We approximate the segregation efficiency as:

$$E \approx \frac{\rho_i L\overline{V}}{Q_s - Q_g} \qquad (22)$$

$$E \approx \frac{\rho_i L\overline{V}}{Q_s - Q_g} = A\frac{Q_s + Q_g}{Q_s - Q_g}\left[\frac{H_{new}}{1 + A(1 - \phi S_{new})} + \frac{H_{max}}{1 + A(1 - \phi S_{max})}\right] \quad (23)$$

where:

$$A = \frac{\rho^2 L^2}{2\mu T_m K_T} \quad (24)$$

$\overline{V}$: Average velocity of segregated ice growth (average heave rate) from Eq.18. The numerator in $Eq. 22$ is the average rate of latent heat consumption by ice lens growth, and the denominator is the total heat flux available to drive lens growth and freezing front progression.

2.6. Scope and Idealized Assumptions

All simulations are conducted under idealized conditions, assuming homogeneous sediment properties, one-dimensional vertical heat and mass transport, and prescribed thermal boundary conditions. These assumptions allow the fundamental controls on ice lens dynamics and segregation efficiency to be isolated and interpreted mechanistically, an approach common in foundational frost heave modeling (Nixon, 1991). This idealized framework is conceptually illustrated in Figure 17, which depicts the one-dimensional soil column with key elements such as the thermal gradient, frozen fringe, ice lens position, and upward water fluxes under open-system conditions (adapted from Nixon, 1991). The diagram highlights the simplified vertical transport and boundary conditions that enable mechanistic isolation of controls on E.

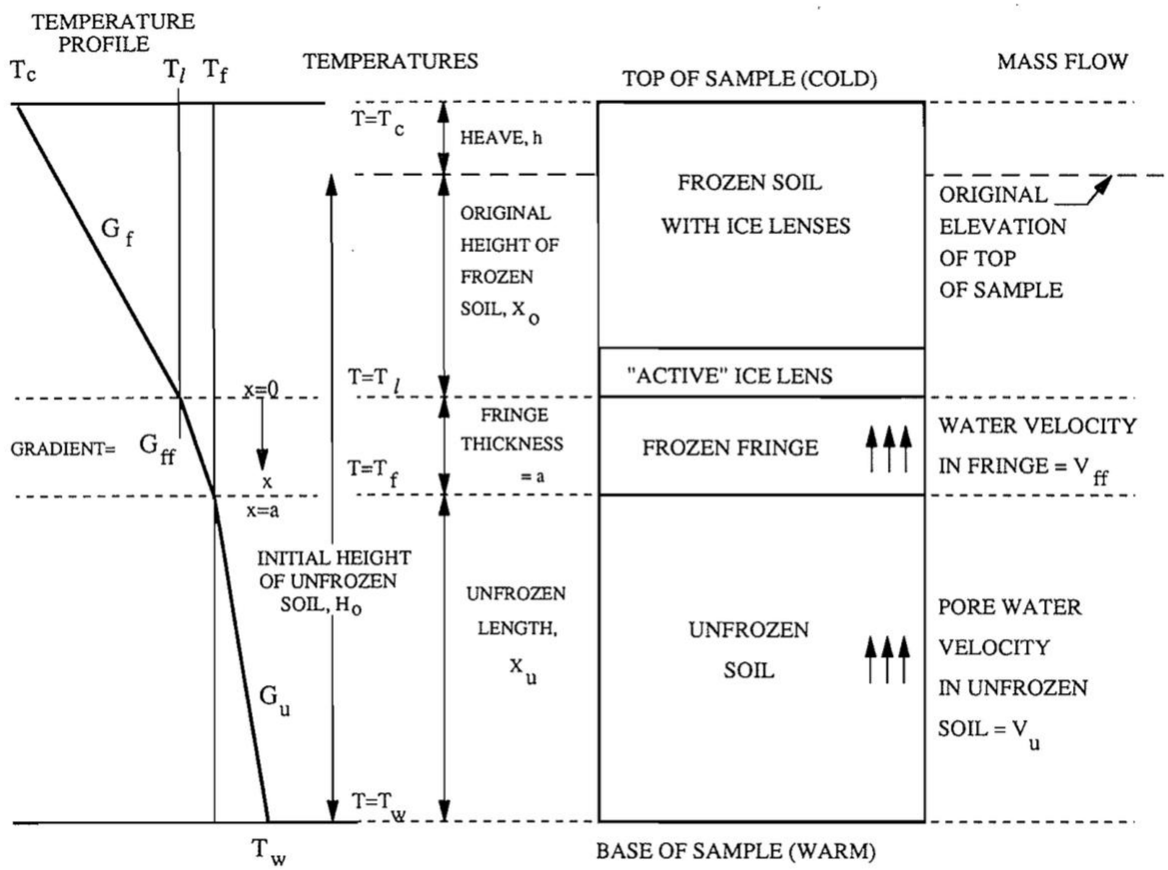

Figure 16. Idealized One-Dimensional Frost Heave Framework.
Idealized one-dimensional schematic of frost heave in a freezing soil column, illustrating temperature gradients, frozen and unfrozen zones, fringe thickness, ice lens position, and upward water fluxes under open-system conditions (reproduced from Nixon, 1991)

While this framework captures the essential physics of frost heave, it does not represent sediment heterogeneity, transient hydrological inputs, or field-scale complexity. These limitations are considered explicitly when interpreting the results and assessing the applicability of segregation efficiency as a scalable parameter for permafrost models.

2.7. Computational Implementation and Numerical Scheme

To maintain computational tractability while resolving discrete ice-lens formation, the model adopts a quasi-steady (quasi-static) approximation rather than a fully transient moving-boundary scheme. Because thermal and hydraulic fields within the thin frozen fringe equilibrate much faster than the seasonal progression of the freezing front, each lens is treated as an equilibrium “event” defined by threshold conditions. Rather than advancing a moving mesh in time, the code solves for the system state at lens initiation using a nonlinear root-finding algorithm (scipy.optimize.fsolve) to determine key temperatures (e.g., $T_{\text{first}}, T_{\text{new}}, T_{\max}$). Lens initiation is identified when the effective interparticle (contact) stress N is zero, indicating that thermomolecular/disjoining forcing can overcome the applied overburden P_0. The nucleation temperature T_{new} is then obtained as the location within the fringe where the critical heaving capacity $H_c(T)$ is maximized, while termination is diagnosed at the corresponding threshold condition defining $T_{\max}$. With these steady-state temperatures, segregation efficiency E is computed from the integrated hydraulic resistance across the fringe (through the permeability–ice-saturation integrals entering H_c and growth-rate expressions). Finally, the imposed surface and geothermal heat fluxes (Q_s, Q_g) are used to close the energy balance and quantify the fraction of available energy diverted into latent heat of segregated ice, enabling efficient parameter sweeps without accumulating long-term transient time-stepping error.

III. RESULTS

The preliminary results presented here illustrate how thermal forcing (surface and geothermal heat flux) and mechanical loading (overburden pressure) control ice lens formation and segregation efficiency under idealized conditions. The simulations focus on a homogeneous sediment column with prescribed surface heat flux and overburden pressure, allowing the fundamental thermomechanical controls on frost heave to be examined while excluding sediment heterogeneity or time-variable hydrologic boundary conditions. We find that ice segregation occurs within a bounded regime of temperature gradients and stresses, beyond which pore freezing dominates and frost heave is suppressed. The lens-resolving framework reproduces the lens-cycle behavior (nucleation–growth–termination; Fig.17) and the resulting range E across imposed thermal forcing and sediment-property scenarios.

We examine ice lens nucleation and growth (Fig.18) using diagnostic measures of heaving capacity, a metric that summarizes the combined thermodynamic driving and hydraulic limitation for supplying water to a lens through the frozen fringe. The conceptual structure of this nucleation–growth–termination cycle is illustrated in Figure 17, which summarizes the coupled thermodynamic and hydraulic controls governing lens evolution. In Figure 18, we show the variation of critical heaving capacity with temperature beneath a growing ice lens. At relatively warm temperatures (small undercooling) near the top of the frozen fringe, the heaving capacity is insufficient to initiate lensing. As temperature decreases (increasing undercooling), increasing cryo-suction enhances the system's ability to draw water toward the freezing front, leading to a peak in heaving capacity that identifies the preferred temperature for new ice lens nucleation (the model's T_{new}). At colder temperatures (greater undercooling), further undercooling reduces permeability (increasing hydraulic resistance across the fringe) due to increased ice saturation, limiting water supply and decreasing the capacity for sustained lens growth. This pattern is consistent with the nucleation–growth–termination cycle described by Rempel (2007), supporting that the model reproduces the key mechanisms of cyclic lens formation under the assumed constitutive relations. This illustrates how sediment properties such as ice saturation (S) and permeability (k), in interaction with thermal gradients, set the range of segregation efficiency (E). The system's ability to transport water through the frozen fringe is further quantified using the heaving capacity associated with an existing ice lens during active growth (Figure 19). This diagnostic reflects how strongly thermodynamic driving (cryo-suction) and hydraulic limitation (permeability) combine to sustain water flux toward the lens for a given thermal gradient. As freezing progresses and the frozen fringe thickens, permeability reduction increasingly restricts water transport, reducing the heaving capacity and slowing lens growth. Overall, the results highlight the central role of permeability evolution in controlling the transition from rapid ice segregation to growth termination. These findings help quantifying the nonlinear influence of porosity (n), ice saturation (S), permeability (k), and thermal gradients on segregation efficiency (E).

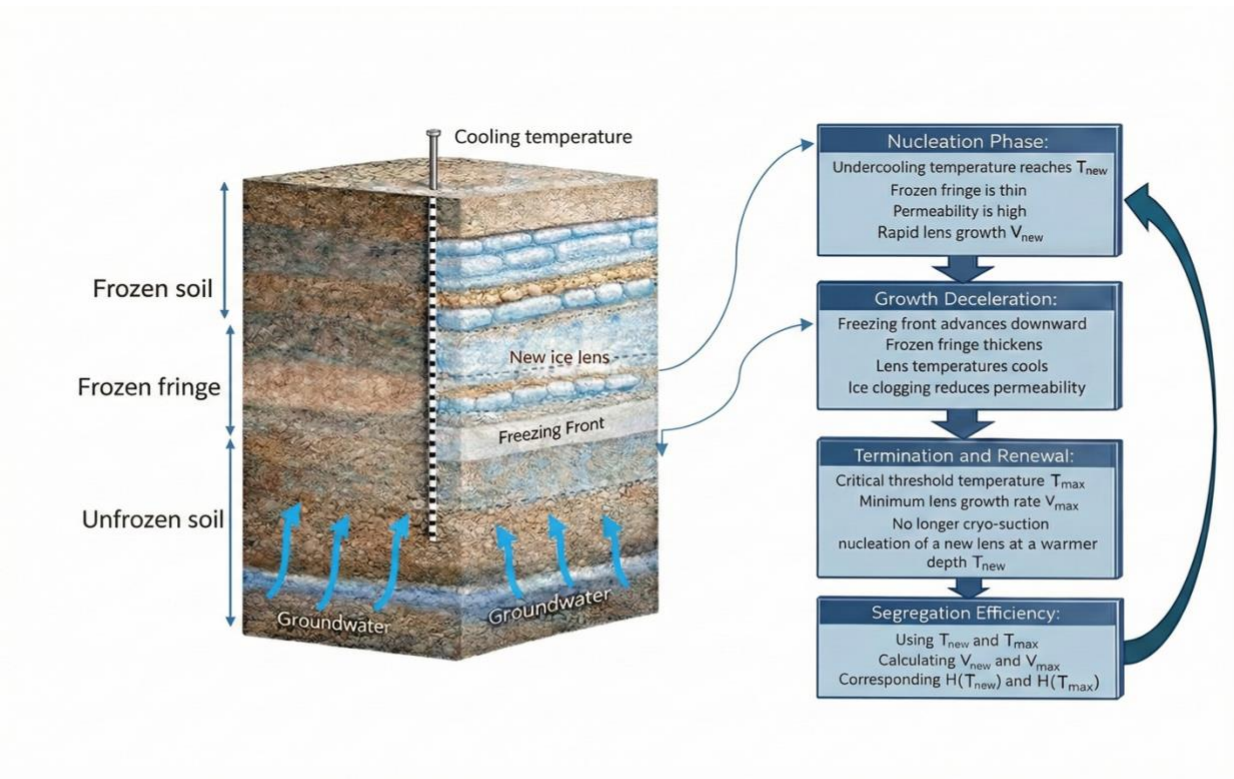

Figure 17. Cyclical Ice Lens Nucleation and Growth Mechanism.

In Figures 18 and 19, $H_c(T)$ is the threshold needed to start lensing, while $H(T)$ is the Actual capacity available to support growth. $H_c(T)$ $H(T)$

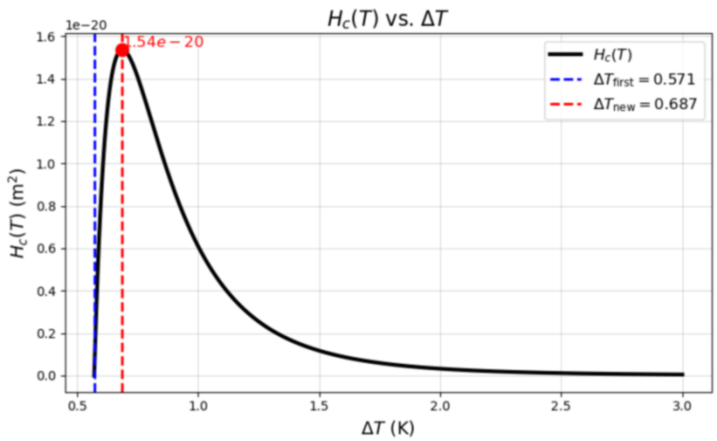

Figure 18. Modeled Critical Heaving Capacity

The diagnostic diagram for ice lens formation derived from numerical simulations for an idealized sample is shown in Figure 18, which depicts the variation of $H_c(T)$ with temperature beneath a growing ice lens. The critical heaving capacity $H_c(T)$ is the threshold value at which a new ice lens can form. Also, it is defined by the product of the heave rate with fringe thickness. The first lens forms where $H_c(T)$ =0. The peak corresponds with ΔT_{new} (subsequent lens initiation), and the H_c at that peak corresponds with the value of H from Fig. 2 to yield ΔT_{max}. Results are based on the implemented model and replicate the behavior shown in Rempel [2007].

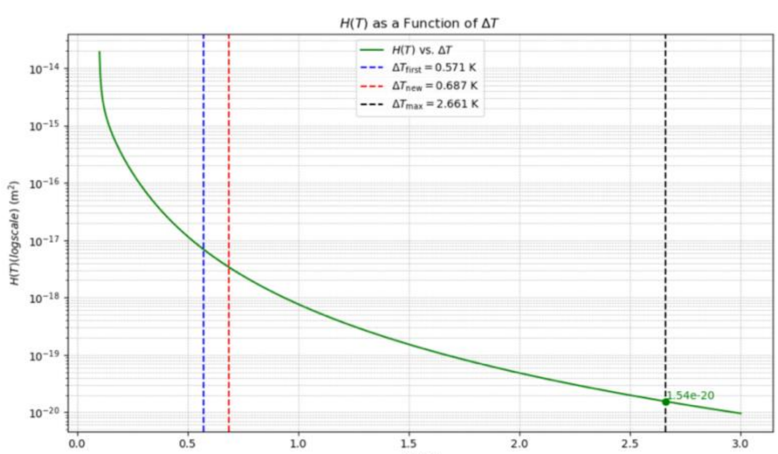

Figure 19. Modeled Heaving Capacity

Figure 19. shows the heaving capacity $H(T)$, which describes the system's capacity to transfer fluid mass toward the freezing front. Here, it quantifies how effectively water can be transported through the frozen fringe to supply lens growth.

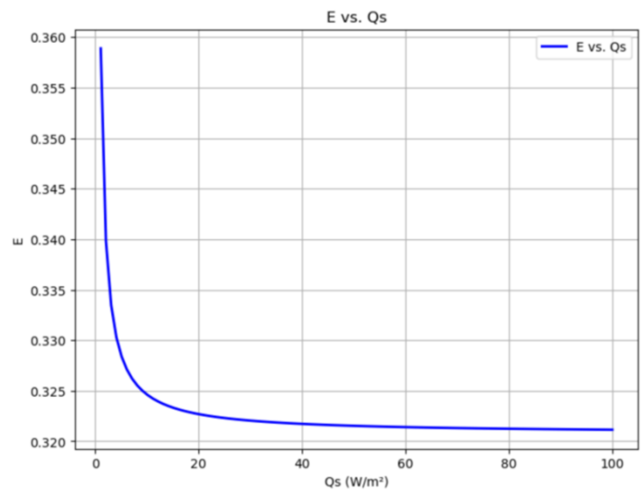

Figure 20. Modeled Segregation Efficiency vs. Surface Heat Flux

The influence of thermal forcing on segregation efficiency is illustrated in Figure 20, which shows the variation of segregation efficiency (E) with imposed surface heat flux (Q_s) under constant geothermal heat flux ($Q_g = 0.06$ W m^{-2}). As the imposed surface heat flux increases, segregation efficiency decreases nonlinearly, indicating that a smaller fraction of the conductive heat removal is converted to latent heat of segregated-ice growth and demonstrating the nonlinear sensitivity of ice segregation capacity to thermal forcing. At high heat fluxes, the fringe becomes colder and more ice-saturated, permeability declines, and water supply to the lens becomes limiting, shifting freezing toward pore-ice formation rather than segregated-ice growth; accordingly, Figure 20 shows how surface heat flux regulates lens formation by suppressing segregated growth at high values. This result demonstrates that segregation efficiency is strongly constrained by the balance between heat removal and hydraulically limited water supply, rather than increasing monotonically with stronger surface cooling. E is calculated using the lens temperatures and heave capacities shown in Fig. 19 under the assumption of a uniform temperature gradient approximated using the average obtained with the different values of Q_s.

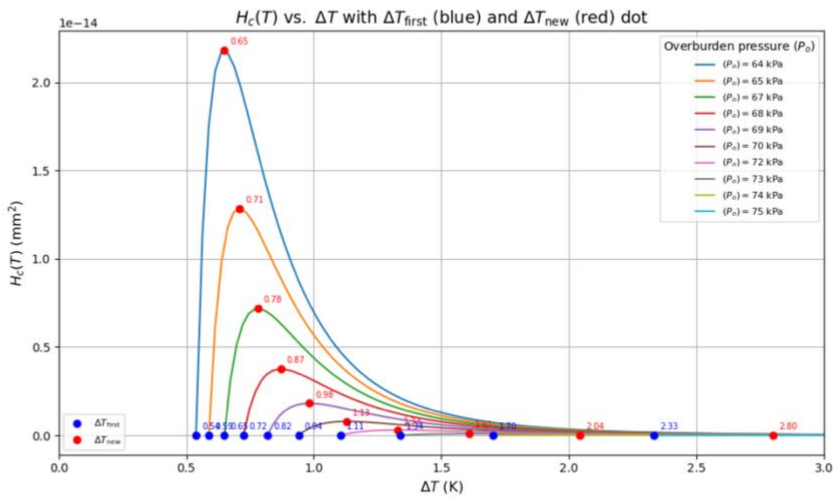

Figure 21. Modeled effect of overburden pressure

Mechanical loading also exerts a strong control on ice lens formation. Figures 21 and 22 show how increasing overburden pressure modifies the nucleation threshold and the peak heaving capacity: as overburden pressure increases, the peak of $H_c(T)$ shifts toward colder temperatures (greater undercooling) and decreases in magnitude, meaning we need a colder temperature (higher ΔT) to initiate lensing, and stronger cryo-suction is required to overcome mechanical resistance. This occurs because the system's ability to drive water to the lens (via $H_c(T)$) drops due to reduced permeability and increased resistance to flow. Figure 22 further shows that ($H(T)$) increases with (P_o) at a given (ΔT), gauging the heave capacity of a given porous system and becoming significant when the force balance causes a reduction in fluid pressure that allows water to be drawn rapidly; ($H(T)$) increases with (P_o) because higher stress means a larger fluid pressure gradient is needed to support ice lensing. These results are consistent with a maximum sustainable heave pressure in the model: beyond a critical overburden stress, the mechanical criterion for lensing is not met, and ice-lens formation is inhibited; at sufficiently high overburden pressures, the system can no longer sustain segregated ice growth, and pore freezing dominates. In Figures 21 and 22, values are shown for overburden pressure (P_o) ranging from 64 to 75 kPa in 1 kPa intervals.

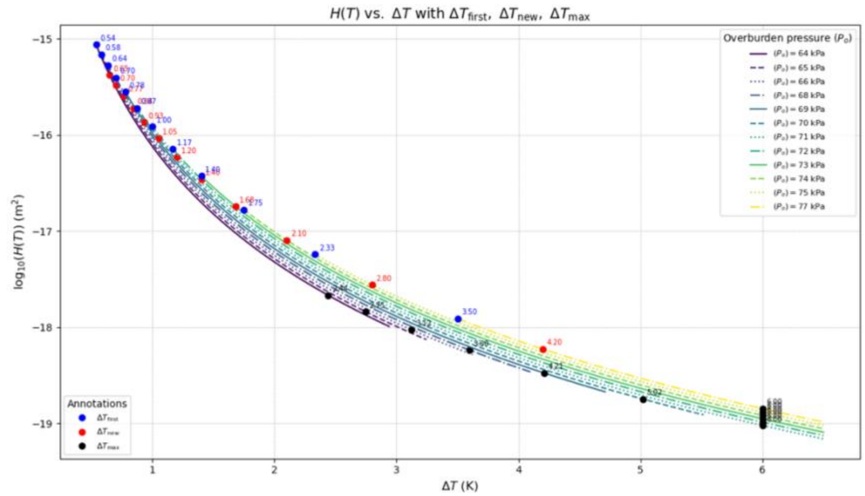

Figure 22. Modeled effect of overburden pressure

Figure 23 further illustrates the dependence of lens nucleation temperature on overburden pressure: increasing mechanical load forces lens nucleation to occur at greater undercooling, reflecting the need for stronger thermodynamic driving forces (cryo-suction) to satisfy the mechanical criterion under higher applied stress.

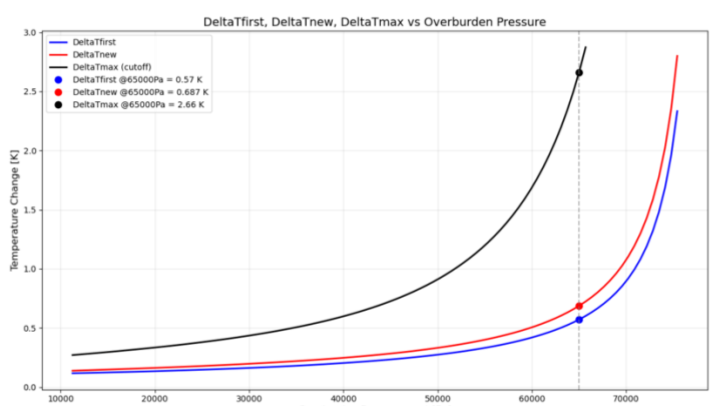

Figure 23. Freezing front temperature as a function of overburden pressure

These results illustrate how mechanical loading controls the thermodynamic thresholds for lens nucleation and reinforce the conclusion that effective stress not only limits the heaving capacity but also governs the thermodynamic conditions under which ice lenses can form, supporting the hypothesis that high effective stress limits segregation efficiency by hindering water migration within the frozen fringe. The vertical dashed line at (P_o= 65) kPa marks the idealized sample illustrated in Figures 19 and 20. Together, these results demonstrate that segregation efficiency and ice lens dynamics emerge from the coupled effects of thermal forcing, permeability evolution, and mechanical loading within the frozen fringe, illustrating the extent to which the lens-resolving model captures temporal changes with limitations noted in idealized conditions.

IV. DISCUSSION

4.1. Interpretation

By explicitly tracking ice saturation and its nonlinear impact on permeability (k), along with imposed mechanical loading, our lens-resolving model shows how segregation efficiency (E) emerges from coupled thermodynamic driving (heat removal and cryo-suction), hydraulic limitation on water supply, and mechanical equilibrium within the frozen fringe. We find that E is bounded between 0 and 1 and, for the parameter ranges explored here, decreases nonlinearly with increasing surface heat flux (Qs), with the strongest sensitivity at low Qs and a gradual leveling at higher Qs. Increasing Qs accelerates conductive heat removal relative to the hydraulically constrained delivery of unfrozen water to an active lens; as freezing progresses, rising ice saturation reduces pore connectivity and permeability, so a smaller fraction of the heat flux is partitioned into latent heat of segregated-ice growth. Consistent with this interpretation, the diagnostic heaving capacity peaks at an intermediate temperature that favors lens nucleation, after which lens growth decelerates and ultimately terminates. This nucleation–growth–termination cycle indicates that frost heave is governed by coupled thermo-hydro-mechanical feedback, consistent with Rempel (2007), and shows that the model reproduces the key mechanisms of cyclic lens formation under the study's idealized assumptions. We further find that mechanical loading shifts ice-lens initiation to colder temperatures and suppresses segregated-ice growth by requiring stronger cryo-suction to overcome the applied stress, thereby narrowing the temperature window for lensing. Above a critical stress threshold, lensing is inhibited and freezing occurs mainly as pore ice (Rempel, 2007), so E depends fundamentally on effective-stress constraint and mechanical feasibility. Since E varies with both thermal forcing and overburden, it is not a fixed soil property but an emergent outcome of coupled heat removal and water supply during freezing. At shorter time scales, experiments suggest pore freezing and ice-lens growth can occur concurrently and that water released during transient freezing may help feed lenses (Akagawa, 1988). However, our quasi-static approach treats the system as a sequence of near-equilibrium states.

Most regional and global permafrost models cannot explicitly resolve the frozen fringe, so ice segregation is typically omitted or represented with simplified parameterizations. Because segregation efficiency (E) is bounded and strongly condition-dependent, treating it as constant or prescribing a monotonic dependence on a single driver can bias predictions of ice accumulation and ground deformation. Although this study does not deliver an implementation-ready parameterization, it provides a mechanistic foundation for constraining E in scalable modeling frameworks using thermal gradients, permeability evolution, and effective stress.

4.2. Limitations and Future Work

Several limitations must be acknowledged. Simulations are idealized (homogeneous sediment, 1-D vertical transport, prescribed thermal boundaries), so they cannot fully capture real-world temporal evolution (RQ3) and motivate multi-dimensional extensions. Real permafrost is heterogeneous (grain size, ice content, hydrology, thermal forcing), and this study omits transient surface forcing, lateral flow, and salinity/solute effects. Experiments show solutes can strongly modify freezing by causing local enrichment (up to threefold) and widening the freezing range ($\Delta U \sim 3$ K vs ~0.05 K) (Ginot et al., 2019), so incorporating solute impacts on frozen-fringe thermodynamics and hydraulic connectivity is an important next step. Water transport is represented with effective hydraulic parameters rather than explicit pore-scale ice–soil interactions (Appendix B Fig. 24), limiting direct field comparison.

Future work should add heterogeneity, transient hydrology, and observational constraints, potentially using "virtual laboratories" such as phase-field (Suh & Sun, 2022) or THM-MPM (Yu et al., 2024) models to test and calibrate E for larger-scale use. Integration into land-surface/ESM frameworks could follow laterally coupled tile approaches (Aas et al., 2019), improving projections of the permafrost-carbon feedback (Aas et al., 2019; Schuur et al., 2015). Extensions should also consider two-sided freezing in permafrost, which concentrates lenses at layer boundaries and may impose distinct spatial constraints on E (Thomas et al., 2009).

Despite these limits, the results show segregation efficiency (E) is a useful bridge from microscale ice-lens growth to macroscale permafrost behavior, clarifying when frost heave is enhanced or suppressed and providing a physically constrained metric that may improve ground-ice initialization and prediction of subsequent thaw consolidation (Liew & Xiao, 2022).

V. CONCLUSION

This thesis uses a lens-resolving frost-heave model to identify how thermodynamic, hydraulic, and mechanical (THM) controls govern ice-lens growth in the frozen fringe and to evaluate segregation efficiency (E) as a scalable metric for permafrost models. Building on Rempel (2007)'s process-based lensing theory, this thesis reframes lens-resolving outputs to quantify segregation efficiency (E). The key result is that E is not a soil constant: it is a bounded, condition-dependent quantity ($0 < E < 1$) that emerges from the coupled effects of thermal gradients (cryo-suction), permeability evolution, and effective stress. Ice segregation is strongest only within a limited temperature-gradient window, where suction can drive water inflow while pore connectivity still permits sufficient hydraulic supply. With greater undercooling, rising ice saturation reduces permeability, water supply becomes limiting, and heat removal increasingly advances pore freezing rather than fueling latent heat from segregated-ice growth—showing that hydraulic limitation is central to frost-heave dynamics. Mechanical loading further constrains lensing: higher overburden shifts nucleation to colder temperatures and suppresses sustained segregated-ice growth, consistent with the concept of a maximum frost-heave pressure (Rempel, 2007). By computing E dynamically from local energy and mass balances, the study links microscale lens processes to macroscale deformation indicators such as heave rates. Overall, the work argues that large-scale models should represent E as bounded and state-dependent, not constant or purely monotonic with cooling rate. While the simulations are idealized (homogeneous sediment, 1-D transport, prescribed boundaries), the framework motivates future testing under heterogeneous, transient conditions, including benchmarking against high-resolution InSAR deformation observations (Sadeghi Chorsi et al., 2024)

SYMBOLS

Parameter	Definition	Unit	Used in Eq.
q	Darcy velocity	m s^{-1}	(3)
C	Specific heat capacity	J kg^{-1} K^{-1}	(14–16)
E	Segregation efficiency	dimensionless	(18)
$H(T)$	Heave capacity	m^2 (scaled proxy)	(13)
$H_c(T)$	Critical heaving capacity	m^2 (scaled proxy)	(12–13)
k	Permeability	m^2	(3), (19)
k_0	Reference/Intrinsic permeability	m^2	(19)
K_1	Thermal conductivity of frozen soil	W m^{-1} K^{-1}	(14–16)
K_2	Thermal conductivity of unfrozen soil	W m^{-1} K^{-1}	(14–16)
K_T	Bulk thermal conductivity	W m^{-1} K^{-1}	(14–16)
L	Latent heat of fusion	J kg^{-1}	(1), (8–10), (16)
N	Effective stress	Pa	(4–7)
P_i	Ice pressure	Pa	(1), (5), (7–10)
P_w	Water pressure	Pa	(1), (3–5)
P_0	Overburden pressure	Pa	(11–13)
Π	Disjoining pressure	Pa	(5), (9–10)
Q_g	Geothermal heat flux	W m^{-2}	(14), (16)
Q_s	Surface heat flux	W m^{-2}	(14), (16)
S	Ice saturation	dimensionless	(20)
T	Local temperature	K	throughout
T_f	Fringe-top temperature	K	(11–13), (19–20)
T_i	Lens temperature	K	(13–16)
T_1	Temperature of frozen soil	K	(thermal section)
T_2	Temperature of unfrozen soil	K	(thermal section)
T_m	Melting temperature	K	(1), (8–10), (19–20)
t	Time	s	(2)
V	Lens growth velocity (Heave Rate)	m s^{-1}	(15–17)
$\bar{V}$	Average lens velocity	m s^{-1}	(17)
α	Permeability exponent	dimensionless	(19)
β	Ice saturation exponent	dimensionless	(20)
κ	Thermal diffusivity	m^2 s^{-1}	(thermal section)
μ	Water viscosity	Pa s	(3), (15–16)
ρ_i	Ice density	kg m^{-3}	(11–13), (16)

Parameter	Definition	Unit	Used in Eq.
ρ_w	Water density	kg m^{-3}	(1), (8–10)
σ_n	Total overburden stress	Pa	(4), (7)
φ	Total porosity	dimensionless	(11–14)
φ_l	Liquid-filled porosity	dimensionless	(2)

APPENDICES

A: CONTEXTUAL COMPARISON WITH PROCESS-RESOLVING MODELS

This appendix presents selected figures from previously published process-resolving thermo–hydro–mechanical simulations to provide qualitative context for the simplified lens-resolving framework employed in this thesis. These figures are not reproduced as results of the present study, nor are they used for quantitative validation. Instead, they serve to illustrate the physical processes resolved by more computationally intensive models and to situate the present approach within the broader hierarchy of frost heave modeling frameworks.

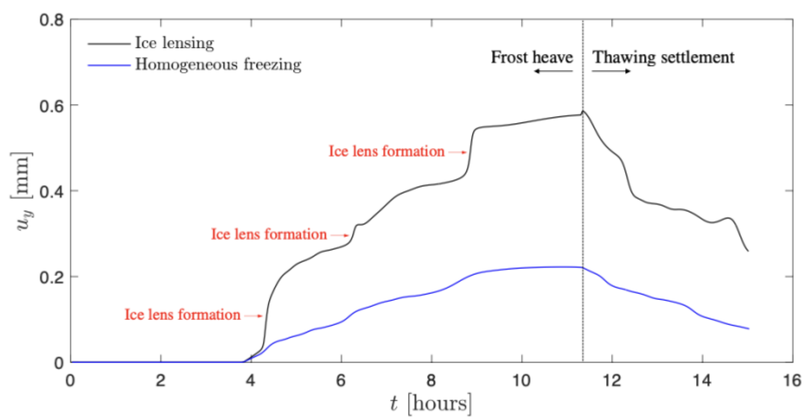

Figure 24. Surface displacement during freeze–thaw.
Time evolution of vertical surface displacement during a numerical freeze–thaw test. The black curve is from a coupled thermo–hydro–mechanical simulation that allows ice lensing, while the blue curve shows an otherwise identical control case in which the ice-lensing mechanism is disabled, resulting in markedly reduced frost heave and subsequent thaw settlement.

In this figure, the black curve corresponds to a process-resolving thermo–hydro–mechanical simulation that permits ice lens formation, while the blue curve represents an otherwise identical control simulation in which ice lensing is suppressed. The figure is shown for qualitative illustration of the role of ice segregation in frost heave and is not intended for quantitative comparison with the results of this thesis.

B: PORE-SCALE ICE–SOIL INTERACTIONS IN THE FROZEN FRINGE

Although water transport in the frozen fringe is represented here using effective hydraulic parameters, detailed pore-scale mechanisms governing ice–soil interactions have been described extensively in the literature.

Water transport through frozen soils is governed by a range of microscale processes occurring at ice–soil interfaces within the frozen fringe. At temperatures below 0 °C, thin premelted water films may persist between ice and mineral surfaces due to intermolecular forces, enabling continued mass transfer despite the presence of pore ice. These films provide connected pathways for water migration toward growing ice lenses and play a role in regulating hydraulic resistance at the grain scale. One mechanism often discussed in the literature is *regelation*, in which stress concentrations at grain contacts induce localized melting of pore ice, followed by meltwater migration and refreezing in regions of lower stress. This process allows pore ice to be effectively advected through the frozen fringe while maintaining overall force equilibrium. Conceptual illustrations of regelation and related interfacial processes are shown in Fig. 25.

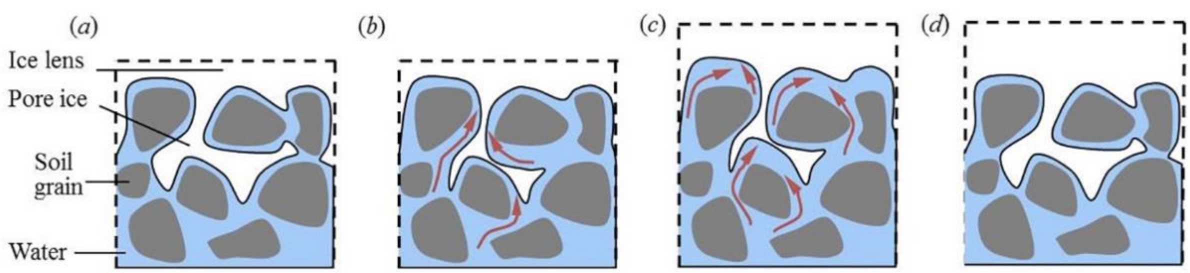

Figure 25. Pore-scale ice–soil interactions.
Conceptual illustration of pore-scale ice–soil interactions within the frozen fringe, including premelted water films and regelation-driven mass transfer at grain contacts. Stress-induced melting, meltwater migration, and refreezing enable continued water transport toward growing ice lenses despite subzero temperatures. Reproduced from / Redrawn after Ice lens induced interfacial hydraulic resistance in frost heave.

In the present thesis, such pore-scale mechanisms are not explicitly resolved. Instead, their cumulative effects are represented using effective hydraulic and thermodynamic parameters, including ice-saturation-dependent permeability and heaving capacity. This homogenized approach enables tractable modeling of ice lens growth and segregation efficiency at the column scale while remaining consistent with established microscale physical interpretations.

C: PERMEABILITY REDUCTION WITH INCREASING FROZEN-PHASE SATURATION

Numerous experimental and pore-scale modeling studies have demonstrated that permeability decreases sharply with increasing solid-phase saturation. Figure 26 illustrates representative permeability reduction curves derived from pore-scale simulations and laboratory measurements, highlighting the strong nonlinearity of permeability loss as ice or hydrate occupies pore space (Chen et al., 2021):

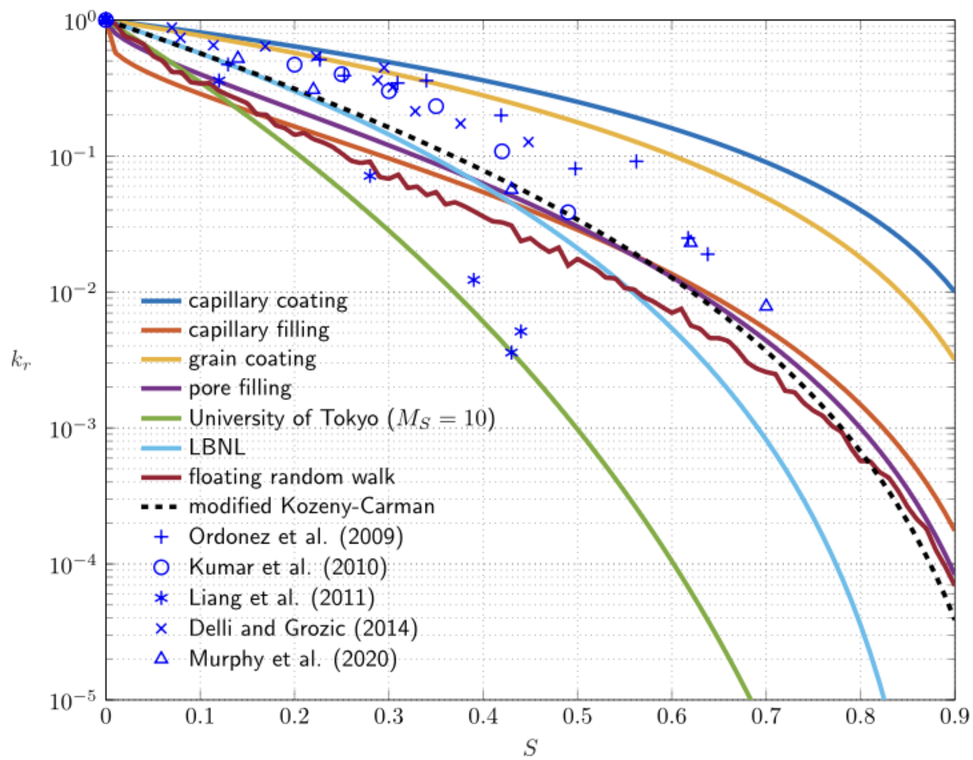

Figure 26. Permeability loss with ice saturation.
Relative permeability declines with increasing frozen-phase saturation. Relative permeability k_r(dimensionless) decreases nonlinearly as frozen-phase saturation Sincreases, indicating progressive hydraulic "sealing" as ice/hydrate occupies pore space. The curves compare several conceptual pore-filling/coating scenarios and commonly used reduction models (including a modified Kozeny–Carman relation) against pore-scale simulation results and published laboratory measurements (symbols) in hydrate-infiltrated porous media. The overall agreement, especially the sharp drop in $k_r$at moderate to high S supports using strongly nonlinear parameterizations for permeability loss within the frozen fringe. (Adapted from Chen et al., 2021, Fig. 4.)

D: NONLINEAR GROWTH OF HYDRAULIC AND ICE-SATURATION INTEGRALS WITH UNDERCOOLING

As illustrated in Figure 27, these integrals exhibit nonlinear growth with undercooling θ (normalized temperature depression), where Γ_1 reflects cumulative ice saturation support across the fringe, and Γ_2 captures escalating hydraulic resistivity due to permeability decline. The ratio $\Gamma_1/\sqrt{\Gamma_2}$ (or derived form) peaks at intermediate θ, indicating the optimal heaving capacity for lens nucleation (T_{new}), which directly influences segregation efficiency E by maximizing water supply before resistance dominates.

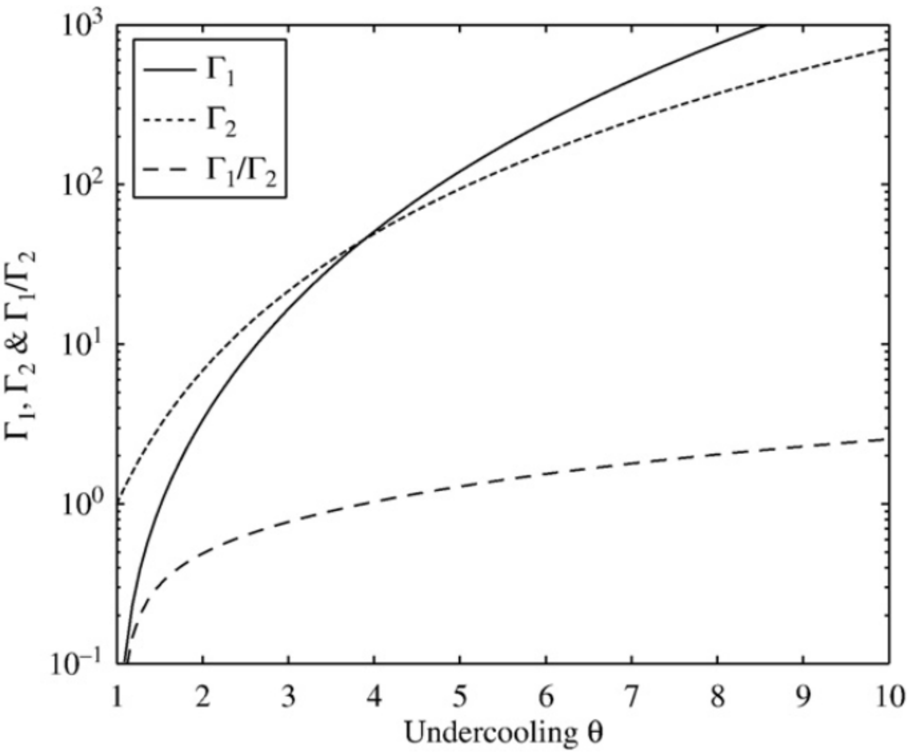

Figure 27. Integrated flow controls vs undercooling.
These relationships for S(T) and k(T) define the key integrals that govern fluid flow and stress in the frozen fringe. Following Rempel (2011), their behavior is encapsulated in the functions $\Gamma_1(\theta)$ and $\Gamma_2(\theta)$ (Fig. 3), which represent the integrated ice saturation and hydraulic resistivity, respectively. Their ratio, Γ_1/Γ_2, scales directly with the heaving capacity H_c and thus controls the temperature of most efficient lens nucleation. (Rempel, 2011)

This visualization, adapted from Rempel (2011), underscores how our power-law parameterizations yield physically constrained bounds on E under varying heat fluxes and sediment types.

REFERENCE

1- Aas, K. S., Martin, L., Nitzbon, J., Langer, M., Boike, J., Lee, H., Berntsen, T. K., & Westermann, S. (2019). Thaw processes in ice-rich permafrost landscapes represented with laterally coupled tiles in a land surface model. The Cryosphere, 13(2), 591–609. https://doi.org/10.5194/tc-13-591-2019

2- Aga, J., Westermann, S., Martin, L. C. P., & Nitzbon, J. (2023). Simulating ice segregation and thaw consolidation in permafrost environments with the CryoGrid community model. The Cryosphere, 17(11), 4179–4206. https://doi.org/10.5194/tc-17-4179-2023

3- Akagawa, S. (1988). Experimental study of frozen fringe characteristics. Cold Regions Science and Technology, 15, 209–223.

4- Arakawa, K. (1966). Theoretical studies of ice segregation in soil. Journal of Glaciology, 6(44), 255–260.

5- Brown, K. M., Hinkel, K. M., & Nelson, F. (2000). The circumpolar active layer monitoring (CALM) program: Research designs and initial results. Polar Geography, 24(3), 166–258.

6- Chen, S., Mei, J. T., Irizarry, T., & Rempel, A. W. (2020a). A Monte Carlo approach to approximating the effects of pore geometry on the phase behavior of soil freezing. Journal of Advances in Modeling Earth Systems, 12(10), e2020MS002117. https://doi.org/10.1029/2020MS002117

7- Chen, J., Wu, Y., O'Connor, M., Cardenas, M. B., Schaefer, K., Michaelides, R., & Kling, G. (2020b). Active layer freeze-thaw and water storage dynamics in permafrost environments inferred from InSAR. Remote Sensing of Environment, 248, 112007. https://doi.org/10.1016/j.rse.2020.112007

8- Chen, S., Mei, J., & Rempel, A. W. (2021). Estimating permeability of partially frozen soil using floating random walks. Water Resources Research, 57(12), e2021WR030598. https://doi.org/10.1029/2021WR030598

9- Clayton, L. K., Schaefer, K., Battaglia, M. J., Bourgeau-Chavez, L., Chen, J., Chen, R. H., Chen, A., Bakian-Dogaheh, K., Grelik, S., Jafarov, E., Liu, L., Michaelides, R. J., Moghaddam, M., Parsekian, A. D., Rocha, A. V., Schaefer, S. R., Sullivan, T., Tabatabaeenejad, A., Wang, K., Wilson, C. J., ... Zebker, H. A. (2021). Active layer thickness as a function of soil water content. Environmental Research Letters, 16(5), 055028. https://doi.org/10.1088/1748-9326/abfa4

10- Cooper, M. G., Zhou, T., Bennett, K. E., Bolton, W. R., Coon, E. T., Fleming, S. W., Rowland, J. C., & Schwenk, J. (2023). Detecting permafrost active layer thickness change from nonlinear baseflow recession. Water Resources Research, 59, e2022WR033154. https://doi.org/10.1029/2022WR033154

11- Dash, J. G., Rempel, A. W., & Wettlaufer, J. S. (2006). The physics of premelted ice and its geophysical consequences. Reviews of Modern Physics, 78(3), 695–741. https://doi.org/10.1103/RevModPhys.78.695

12- Devoie, E. G., Gruber, S., & McKenzie, J. M. (2022). A repository of measured soil freezing characteristic curves: 1921 to 2021. Earth System Science Data, 14(7), 3365–3377. https://doi.org/10.5194/essd-14-3365-2022

13- Fu, Z., Wu, Q., Zhang, W., He, H., & Wang, L. (2022). Water migration and segregated ice formation in frozen ground: Current advances and future perspectives. Frontiers in Earth Science, *10*, 826961. https://doi.org/10.3389/feart.2022.826961

14- Fukuda, M., & Kinosita, S. (1985). Field frost heave prediction related to ice segregation processes during soil freezing. Annals of Glaciology, 6, 87–91. https://doi.org/10.3189/1985AoG6-1-87-91

15- Ginot, F., Lenavetier, T., Dedovets, D., & Deville, S. (2019). Solute effects in confined freezing. arXiv. https://arxiv.org/abs/1907.10502v1

16- Gruber, S. (2020). Ground subsidence and heave over permafrost: Hourly time series reveal interannual, seasonal, and shorter-term movement caused by freezing, thawing, and water movement. The Cryosphere, 14(4), 1437-1447. https://doi.org/10.5194/tc-14-1437-2020

17- Heginbottom, J. A., Brown, J., Humlum, O., & Svensson, H. (2012). Permafrost and periglacial environments. In R. S. Williams, Jr., & J. G. Ferrigno (Eds.), Satellite image atlas of glaciers of the world: State of the Earth's cryosphere at the beginning of the 21st century: Glaciers, global snow cover, floating ice, and permafrost and periglacial environments (U.S. Geological Survey Professional Paper 1386–A–5). U.S. Geological Survey. https://pubs.usgs.gov/pp/1386a/

18- Hjort, J., Karjalainen, O., Aalto, J., Westermann, S., Romanovsky, V. E., Nelson, F. E., Etzelmüller, B., & Luoto, M. (2018). Degrading permafrost puts Arctic infrastructure at risk by mid-century. Nature Communications, 9(1), 5147. https://doi.org/10.1038/s41467-018-07557-4

19- Ji, Y., Zhou, G., Zhou, Y., & Vandeginste, V. (2019). Frost heave in freezing soils: A quasi-static model for ice lens growth. Cold Regions Science and Technology, 158, 1–14. https://doi.org/10.1016/j.coldregions.2018.11.003

20- Kjelstrup, S., Ghoreishian Amiri, S. A., Loranger, B., Gao, H., & Grimstad, G. (2021). Transport coefficients and pressure conditions for growth of ice lens in frozen soil. Acta Geotechnica, 16, 2231–2239. https://doi.org/10.1007/s11440-021-01158-0

21- Konrad, J. M., & Morgenstern, N. R. (1981). The segregation potential of a freezing soil. Canadian Geotechnical Journal, 18(4), 482–491.

22. Kurylyk, B. L., & Hayashi, M. (2016). Improved Stefan equation correction factors to accommodate sensible heat storage during soil freezing or thawing. Permafrost and Periglacial Processes, 27(2), 189–203. https://doi.org/10.1002/ppp.1865

22- Liew, M., & Xiao, M. (2022). Three-dimensional fully coupled thermo-hydro-mechanical model for thaw consolidation of permafrost. Journal of Geotechnical and Geoenvironmental Engineering, 148(11), 04022105. https://doi.org/10.1061/(ASCE)GT.1943-5606.0002917

23- López-Chacón, S. R., Salazar, F., & Bladé, E. (2023). Combining synthetic and observed data to enhance machine learning model performance for streamflow prediction. Water, 15(2020).

24- Meyer, C. R., Schoof, C., & Rempel, A. W. (2023). A thermomechanical model for frost heave and subglacial frozen fringe. Journal of Fluid Mechanics, 964, Article A42. https://doi.org/10.1017/jfm.2023.366

25- Murton, J. B., Peterson, R., & Ozouf, J.-C. (2006). Bedrock fracture by ice segregation in cold regions. *Science, 314*(5802), 1127–1129. https://doi.org/10.1126/science.1132127

26- Nixon, J. F. (1991). Discrete ice lens theory for frost heave in soils. Canadian Geotechnical Journal, *28*(6), 843–859.

27- Nelson, F. E., Shiklomanov, N. I., & Nyland, K. E. (2021). Cool, CALM, collected: The Circumpolar Active Layer Monitoring program and network. Polar Geography, 44(3), 155–166. https://doi.org/10.1080/1088937X.2021.1988001

28- Nitzbon, J., Krinner, G., Schneider von Deimling, T., Werner, M., & Langer, M. (2023). First quantification of the permafrost heat sink in the Earth's climate system. Geophysical Research Letters, 50(11), e2022GL102053. https://doi.org/10.1029/2022GL102053

29- Peppin, S. S. L. (2022). Ice segregation efficiency theory of frost heave. OSF Preprints. https://doi.org/10.31219/osf.io/vh4n5

30- Rempel, A. W., Wettlaufer, J., & Worster, M. G. (2004). Premelting dynamics in a continuum model of frost heave. Journal of Fluid Mechanics, 498, 227–244. https://doi.org/10.1017/S0022112003007010

31- Rempel, A. W. (2007). Formation of ice lenses and frost heave. Journal of Geophysical Research: Earth Surface, 112(F2), F02S21. https://doi.org/10.1029/2006JF000525

32- Rempel, A. W. (2011). Microscopic and environmental controls on the spacing and thickness of segregated ice lenses. Quaternary Research, 75(3), 316–324. https://doi.org/10.1016/j.yqres.2010.07.005

33- Sadeghi Chorsi, T., Meyer, F. J., & Dixon, T. H. (2024). Toward long-term monitoring of regional permafrost thaw with satellite interferometric synthetic aperture radar. The Cryosphere, 18(8), 3723–3740.

34- Smith, S. L., O'Neill, H. B., Isaksen, K., Noetzli, J., & Romanovsky, V. E. (2022). The changing thermal state of permafrost. Nature Reviews Earth & Environment, 3(1), 10–28. https://doi.org/10.1038/s43017-021-00240-6

35- Schuur, E. A. G., McGuire, A. D., Schädel, C., Grosse, G., Harden, J. W., Hayes, D. J., Hugelius, G., Koven, C. D., Kuhry, P., Lawrence, D. M., Natali, S. M., Olefeldt, D., & Turetsky, M. R. (2015). Climate change and the permafrost carbon feedback. Nature, 520(7546), 171-179. https://doi.org/10.1038/nature14338

36- Stubblefield, A. G., Meyer, C. R., Rempel, A. W., Warburton, K. L. P., Hansen, D. D., & Zoet, L. K. (2025). Modelling sediment compaction beneath ice lenses during frost heave. Proceedings of the Royal Society A: Mathematical, Physical and Engineering Sciences, 481(2310), 20240516. https://doi.org/10.1098/rspa.2024.0516

37- Suh, H. S., & Sun, W. (2022). Multi-phase-field microporomechanics model for simulating ice-lens growth in frozen soil. International Journal for Numerical and Analytical Methods in Geomechanics, *46*, 2307–2336. https://doi.org/10.1002/nag.3408

38- Taber, S. (1929). Frost heaving. The Journal of Geology, 37(5), 428–461.

38- Taber, S. (1930). The mechanics of frost heaving. Journal of Geology, 38(4), 303–317.

39- Thomas, H. R., Cleall, P., Li, Y.-C., Harris, C., & Kern-Luetschg, M. (2009). Modelling of cryogenic processes in permafrost and seasonally frozen soils. Geotechnique, 59 (3), 173–184.https://doi.org/10.1680/geot.2009.59.3.173

40- Turetsky, M. R., Abbott, B. W., Jones, M. C., Anthony, K. W., Olefeldt, D., Schuur, E. A. G., Grosse, G., Kuhry, P., Hugelius, G., Koven, C., Lawrence, D. M., Gibson, C., Sannel, A. B. K., & McGuire, A. D. (2020). Carbon release through abrupt permafrost thaw. Nature Geoscience, 13(2), 138–143. https://doi.org/10.1038/s41561-019-0526-0

41- Yang, G., Chen, P., & Cai, G. (2021). Nonlinear analysis of the thaw settlement in ice-rich embankments. Mathematical Problems in Engineering, 2021, Article 5561302. https://doi.org/10.1155/2021/5561302

42- Yu, J., Zhao, J., Zhao, S., & Liang, W. (2024). Thermo-hydro-mechanical coupled material point method for modeling freezing and thawing of porous media. International Journal for Numerical and Analytical Methods in Geomechanics, 48(13), 3308–3349. https://doi.org/10.1002/nag.3794

43- Zhou, J., & Wei, C. (2020). Ice lens-induced interfacial hydraulic resistance in frost heave. Cold Regions Science and Technology, 171, 102964. https://doi.org/10.1016/j.coldregions.2019.102964